LUND UNIVERSITY
Faculty of Science

Electric Field Domains in Quantum Cascade Lasers

Tim Almqvist

Thesis submitted for the degree of Master of Science
Project duration: 9 months

Supervised by Prof. Andreas Wacker

Department of Physics
Division of Mathematical Physics
January 2017

Abstract

Quantum cascade lasers (QCLs) are periodic semiconductor heterostructures, capable of producing laser gain. They have become an important source of coherent radiation in the mid infrared, and THz frequency regions. QCLs are non-linear electric devices, and often have bias regions of negative differential resistivity (NDR). These regions are inherently unstable, and electric field domains (EFDs) form in the structure. They are spatial regions with distinct different electric field strengths. These EFDs have a large impact on the behaviour of the device within the regions of NDR.

A theoretical model for describing electron transport in superlattices is discussed and extended upon. This model is also adapted for QCLs, and implemented in a simulation program in order to investigate the dynamics of the EFDs. The program considers few hundred periods, where the behaviour of a single period is obtained beforehand via a program using a non-equilibrium Green's function (NEGF) model. Simulations have been performed using the theoretical model, and compared to experimental results. The simulated results include the electric field strength and electron densities, which are resolved in both space and time, for various externally applied biases. Also the time resolved current and bias across the QCL are calculated.

Results have been obtained in good agreement with experiments at higher temperatures, while bias oscillations observed at low temperatures in experiments could not be reproduced in simulations with identical conditions. Simulations with an increased capacitance show a significant impact on pulsed mode operation. Employing an external capacitance in experiments could improve the ability to resolve a plateau with stable EFDs. With a reduced current, bias oscillations have been observed in simulations and analysed. Characteristic shapes of current and bias oscillations have been related to the dynamics of EFDs. Oscillations with good qualitative agreement with experiments have been observed, while the time scale of the oscillations deviated with less than an order of magnitude.

Acknowledgements

I would like to thank my supervisor, Andreas Wacker for his encouraging words and always making me feel like i was doing something of value. I am also very grateful that he invited me to the International Quantum Cascade Laser School and Workshop 2016, that took place in Cambridge. It was very enjoyable, and I learnt a lot during that week.

I would like to thank David Winge for all the help, for answering my numerous questions, and for the many valuable discussions throughout this project. I also want to thank Martin Frankie for introducing me to the NEGF program, and both him and the rest of the group for interesting discussions.

Finally, i want to thank Emmanuel Dupont for providing experimental data and giving me the permission to use them in my thesis.

Contents

List of Acronyms

EFD electric field domain

NDR negative differential resistivity

NEGF non-equilibrium Green's function

QCL Quantum cascade laser

1 Introduction

A superlattice is a heterostructure that is grown with thin, alternating layers of semiconductor materials. Due to the different band gaps of the semiconductors, the electrons in the conduction band will feel rectangular potential wells and barriers in the growth direction, called quantum wells. Superlattices are typically n-doped, in order to put electrons into the conduction band. With modern epitaxy the superlattice layers can be grown thin enough to create bound electron states within these wells.

When a bias is applied to a superlattice, along the growth direction, the ground state energy within the square wells will be successively lower for each well, as shown in figure 2.1. For small biases this will create a tunnelling current through the superlattice, where electrons tunnel from the ground state in one well to the ground state in the next. However, when the bias is further increased, the ground states in the quantum wells are no longer aligned in energy, which causes a reduced tunnelling current. This type of region where the current goes down with increasing bias is usually referred to as a negative differential resistivity (NDR) region. At even higher biases, the ground state in one well will become aligned with the first excited state in the next one. When this happens, the current once again increases.

Superlattices are capable of producing so called Bloch gain [1], which, in theory, could be exploited for stimulated emission of electromagnetic radiation. However, since this occurs in a NDR region, it has so far not been possible to realise in practice. The reason for this is that NDR regions are inherently unstable when a large number of periods are considered. Instead of having a uniform electric field which corresponds to a bias within the region of NDR, two distinct domains with different electric field strengths form. The electric fields in these two electric field domains (EFDs) correspond to a bias below and above the NDR region, neither of which produces gain.

Quantum cascade lasers (QCLs) are periodic heterostructure devices, similar to superlattices, that are carefully designed to produce gain. In contrast to superlattices, they typically have a period consisting of several quantum wells and barriers. By designing the periodicity such that population inversion between two bound states are obtained once per period, gain can be obtained in a positive differential resistivity region. The laser transition thus takes place inside the conduction band. This is fundamentally different from a diode laser, where the laser transition takes place between bands.

Since the first successful demonstration in 1994 [2], QCLs have become an important source of coherent radiation in the mid and far infrared regions. One of the main challenges in current research is increasing the maximum operational temperature, and the output power at higher temperatures. This is particularly true for far infrared QCLs, also referred to as THz QCLs, for which the best structure has only reached a maximum lasing temperature of 200 K [3].

Although typically not desirable, many QCLs also have NDR regions which cause formation of EFDs. When these occur at or above the lasing threshold bias, they could affect the properties of the QCL. Therefore, simulations of EFDs are required for explaining their behaviour accurately. Further, simulations of EFDs would allow investigation of exploiting EFDs for laser ignition. This is an intriguing possibility that could increase the operation temperature of the QCL.

As EFDs form in the NDR region, a minimum in the current as a function of bias is not observed in experiments. Therefore, within these regions it is difficult to evaluate the accuracy of models that consider a uniform electric field. Simulating EFDs allows a comparison between the simulated and experimental current also within the regions of NDR. Further, as argued in [4], the dynamics of EFDs are sensitive to the depth and width of the minimum. Simulating the dynamics of EFDs could provide a method for evaluating the accuracy of models, considering a uniform field, within these regions.

In section 2, a theoretical model for electron transport in periodic semiconductor heterostructures is described. Section 3 describes how the model from chapter 2 is implemented in a simulation program. Section 4 presents the first results, using a constant bias across the QCL. In section 5 the results of the simulations with the experimental circuit and various contact conductance are presented, and compared to experiments. Section 6 discusses the impact of an external capacitance on QCLs operated in pulsed mode. Finally section 7 provides a short summary of the project, as well as an outlook on further research directly related to this project.

2 Electron Transport in Periodic Semiconductor Heterostructures

In this section, the model for electron transport in a superlattice is described, following [4]. Figure 2.1 shows the lower band edge of the conduction band for such a structure, with an applied external bias. n_i is the electron density in the i:th well, and F_i is the electric field across the barrier between well i and $i+1$. The current density through a barrier strongly depends on the local electric field and the number of occupied states in the initial and final wells. Assume for now that the current from well i to $i+1$ is given by some known function: $J_{i\to(i+1)} = J(F_i, n_i, n_{i+1})$. Note that there is an implicit time dependence for all electron densities, currents, electric fields and biases.

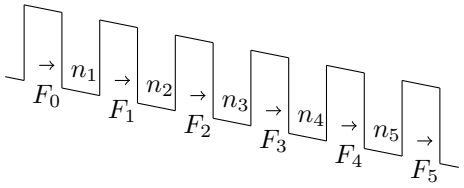

Figure 2.1: The black lines represent the lower band edge of the conduction band of a superlattice with $N = 5$ wells and $N + 1 = 6$ barriers. The bands are tilted due to an externally applied bias. n_i represents the number of electrons in well i, and F_i represents the local electric field across the barrier between well i and $i + 1$.

Given the current density through each barrier we can find the time derivative of the electron densities from the continuity equation:

$$e\frac{dn_i}{dt} = J_{(i-1)\to i} - J_{i\to(i+1)} \qquad i = 1, 2, \ldots, N \tag{2.1}$$

where e is the electron charge. Further, discretising the Poisson equation for electric fields in the superlattice yields:

$$\varepsilon(F_i - F_{(i-1)}) = e(n_i - N_d) \qquad i = 1, 2, \ldots, N \tag{2.2}$$

where N_d is the doping density, and ε is the permittivity. This can clearly not be solved for $i = 0$ as there is no well before the first barrier. Hence, we also need the following equation in order to be able to solve the set of equations:

$$U = \sum_{i=0}^{N} F_i d \tag{2.3}$$

where d is the width of each period in the superlattice, and U is the bias across the entire structure. For the case of a constant total bias, these three equations, combined with appropriate boundary conditions for $J_{0\to1}$ and $J_{N\to N+1}$, allows for a complete description of the temporal evolution of the system. However, there is an alternative approach for describing the system where the time derivatives of the electric fields are explicitly defined:

$$\varepsilon\frac{dF_i}{dt} = J - J_{i\to(i+1)} \qquad i = 0, 1, \ldots, N \tag{2.4}$$

where J is the total current density, given by:

$$(N+1)J = \sum_{i=0}^{N} J_{i\to(i+1)} + \frac{\varepsilon}{d}\frac{dU}{dt} \ . \tag{2.5}$$

The electron densities can then be expressed as:

$$n_i = N_d + \frac{\varepsilon}{e}(F_i - F_{i-1}) \quad i = 1, 2, ..., N. \tag{2.6}$$

It is noteworthy that equation (2.1) contains N differential equations, in contrast to equation (2.4) which contains $N+1$. The N differential equations for the densities are, in fact, sufficient for describing the system. However, this difference will be important when a time dependent bias is introduced in section 2.1.

In order to obtain a closed set of equations for the temporal evolution of the system, appropriate boundary conditions for the current density through the first and the last barriers, e.g. $J_{0\to1}$ and $J_{N\to(N+1)}$, are required. One approach, that will be referred to as *constant density* boundary condition, is to define constant electron densities in fictitious wells before the first barrier and after the last barrier. This allows the calculation of $J_{0\to(0+1)}$ and $J_{N\to(N+1)}$ by the same means as the other current densities.

An alternative approach is to assume that the current is proportional to the local electric field across the first and final barriers. This will be referred to as *Ohmic* boundary conditions, as it is given by $J_{0\to1} = \frac{\sigma F_0 d}{A}$, where σ is the Ohmic conductance, and A is the contact area. However, for the final barrier, some precaution must be taken to avoid a negative electron density in the last well. A reasonable way to accomplish this is to make the current density proportional to the electron density in the last well: $J_{N\to(N+1)} = \frac{n_N \sigma F_N d}{N_d A}$.

Let us return to the problem of finding the current through each barrier, given the electric field across the barrier and the electron densities in nearby wells. An expression for this current has been derived in [5]:

$$J_{i\to(i+1)} = \frac{e\, v(F_i)}{d\left(1 - \mathrm{e}^{-(eF_i d/k_B T)}\right)} \left[n_i - \frac{m^* k_B T}{\pi\hbar^2} \ln\left(1 + \mathrm{e}^{-(eF_i d/k_B T)}(\mathrm{e}^{\pi\hbar^2 n_{i+1}/m^* k_B T} - 1)\right)\right] \tag{2.7}$$

which, in the limiting case $T \gg \pi\hbar^2 n_{i+1}/m^* k_B$, can be approximated by:

$$J_{i\to(i+1)} \approx \frac{e\, v(F_i)}{d} \frac{n_i - n_{i+1}\,\mathrm{e}^{-(eF_i d/k_B T)}}{1 - \mathrm{e}^{-(eF_i d/k_B T)}} \ , \tag{2.8}$$

where $v(F)$ is the average drift velocity [4]:

$$v(F) = \frac{d}{eN_d} J(F, N_d, N_d) \ . \tag{2.9}$$

Now the problem has been reduced to finding $J(F, N_d, N_d)$ which only depends on one variable, as the doping density N_d is constant. This quantity is one of the main results from the simulation program based on the non-equilibrium Green's function (NEGF) model [6].

Although the model described here has been developed for superlattices, it is fairly straight forward to adapt it for QCLs. Due to the periodicity of the QCL, the average current density

through a period is the same, independent of where the border between periods is considered to be. Assuming that the electrons accumulate at the same z-position within each period, each barrier in figure 2.1 can be replaced with a sequence of barriers that appears in each period in the QCL. Therefore, by using the effective current density through one period of the QCL as $J(F, N_d, N_d)$, the model can be used to investigate the time dependence of EFDs in QCLs.

2.1 Experimental Circuit

In order to compare the simulated results to experimental measurements, it is desirable to simulate the entire experimental setup, in contrast to having a constant bias across the QCL. As seen in figure 2.2 a), the main components are a source of constant bias U_0 connected in series with a resistor, with resistance R, and the QCL. Additionally there may be some external capacitance, C_{ext}, in the circuit. The total current J is now given by Ohm's law for the current through the resistor:

$$A \cdot J = \frac{U_0 - U}{R} \ . \tag{2.10}$$

A similar setup is considered in [7], where an expression for $\frac{dU}{dt}$ is derived. Let z denote the growth direction of the QCL, and let x and y expand the plane perpendicular to z. Using Ampere's law for the surface shown with dashed lines in figure 2.2 b), the following expression is obtained:

$$\frac{C_{\text{ext}}}{\varepsilon(z)} \frac{dU}{dt} + \iint_A \left(\frac{dF_z}{dt} + \frac{j_z}{\varepsilon(z)} \right) dx\, dy - \frac{A \cdot J}{\varepsilon(z)} = 0 \ . \tag{2.11}$$

F_z and j_z are now the z components of the electric field and the current density, respectively, at any point in space. The electric field and current density are also assumed to not have any x or y components, which is reasonable for the considered geometry.

The above expression is integrated over the length of the QCL in the z direction:

$$\frac{dU}{dt} = \frac{1}{C_{\text{QCL}} + C_{\text{ext}}} \left(A\, J - \frac{C_{\text{QCL}}}{A} \iint_A dx\, dy \int_0^L dz \frac{j_z}{\varepsilon(z)} \right) \tag{2.12}$$

where C_{QCL} is the intrinsic capacitance of the QCL, and is given by:

$$C_{\text{QCL}}^{-1} = \int_0^L dz \frac{1}{A\, \varepsilon(z)} \ . \tag{2.13}$$

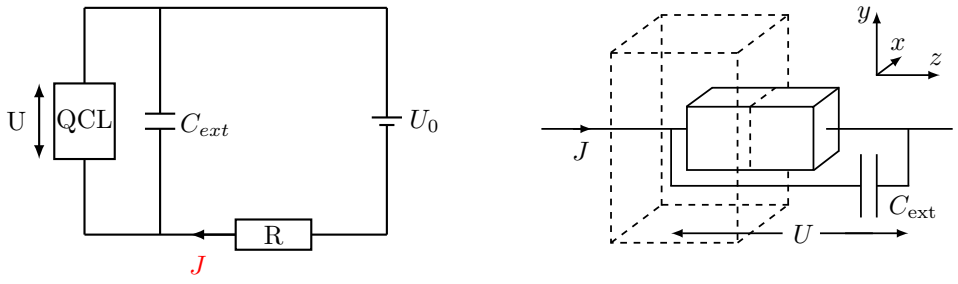

Figure 2.2: a) Schematic of the experimental setup of an operating QCL. b) Zoomed in on the QCL and the external capacitor, showing the surface of integration with dashed lines. Figure inspired by reference [7].

Since there is no x or y dependence, the double integral in equation (2.12) simply becomes A, the cross section area of the QCL.

Using the above equations, derived in [7], we can apply them for the specific scenario considered here. Assuming that the permittivity, ε, is independent of z, an explicit expression for the intrinsic capacitance of the QCL is obtained:

$$C_{\mathrm{QCL}} = \frac{A\,\varepsilon}{d(N+1)} \ , \tag{2.14}$$

and the integral over z in equation (2.12) can be written as a sum over the QCL periods:

$$\int_0^L dz \frac{j_z}{\varepsilon(z)} = \frac{d}{\varepsilon} \sum_{i=0}^{N} J_{i\to i+1} \ . \tag{2.15}$$

Inserting these two relationships into equation (2.12) we obtain:

$$\frac{C}{A}\frac{dU}{dt} = J - \frac{1}{N+1} \sum_{i=0}^{N} J_{i\to i+1} \tag{2.16}$$

where $C = C_{\mathrm{QCL}} + C_{\mathrm{ext}}$ is the total capacitance. This equation can now be used to numerically integrate the total bias across the QCL, where the total current J is given by equation (2.10). Combining this with the differential equations for the electron densities, the time evolution of the entire system can be described. Just as before equations (2.2) and (2.3) are used to obtain the electric fields, F_i.

In order to obtain $\frac{dF_i}{dt}$ for an arbitrary period within the QCL, equation (2.11) is integrated over the length of that period:

$$\int_{d\cdot i}^{d\cdot(i+1)} dz \left(\frac{C_{\mathrm{ext}}}{\varepsilon(z)} \frac{dU}{dt} + A\frac{dF_z}{dt} + A\frac{j_z}{\varepsilon(z)} - A\frac{J}{\varepsilon(z)} \right) = 0 \ , \tag{2.17}$$

which yields:

$$\varepsilon \frac{dF_i}{dt} = J - J_{i\to i+1} - \frac{C_{\mathrm{ext}}}{A}\frac{dU}{dt} \ . \tag{2.18}$$

Now we insert equation (2.16) into this equation:

$$\varepsilon \frac{dF_i}{dt} = J - J_{i\to i+1} - \frac{C_{\mathrm{ext}}}{C} \left(J - \frac{1}{N+1} \sum_{i=0}^{N} J_{i\to i+1} \right) \ . \tag{2.19}$$

This equation now replaces equation (2.4), for the alternative approach. A new bias, U, is then given by (2.3), and the electron densities, n_i, are given by equation (2.6). This model gives $N+1$ identical differential equations, compared to the first approach, which has N differential equations for the electron densities and one for the bias, U.

3 Simulating Electric Field Domains in Quantum Cascade Lasers

A `C++` program implementing the model described in section 2 was written. The goal of this program is to investigate the formation and dynamics of EFDs in QCLs, hence it will be referred to as the *EFD program*. The program relies on two input files. The first one contains parameters that are undesirable to define at compile time. The second input file contains a list of values for $J(F, N_d, N_d)$ and F spaced over the range of field strengths of interest.

The EFD program begins with a flat configuration of electric field strengths, e.g. $F_i^0 = \frac{U}{(N+1)d}$ for $i = 0, 1, ...N$, and the starting electron density in each well is equal to the doping density, $n_i^0 = N_d$ for $i = 1, 2, ...N$. Here the superscript is used to denote the point in time. After defining the initial conditions the EFD program immediately advances to the inner loop as can be seen in the flowchart in figure 3.1. This loop does four things: increment the time t with a small delta time h, calculate n_i^{t+h} and F_i^{t+h}, calculate $J_{i\to(i+1)}^{t+h}$, and check if a stationary configuration has been reached. The loop ends when either, the current EFD configuration is stationary, or some maximum time t_{max} is reached.

As discussed in section 2, there are two approaches for calculating n_i^{t+h} and F_i^{t+h}. The first method numerically integrates each n_i using equation (2.1). Subsequently each F_i is computed using equations (2.2) and (2.3). The second approach is to numerically integrate each F_i using (2.4). Assuming a constant total bias, equation (2.5) can be used to obtain J. Thereafter, each n_i is computed using (2.6). Both approaches have been implemented in the EFD program, with both Euler and fourth order Runge-Kutta integration algorithms.

$J_{i\to(i+1)}^{t+h}$ are calculated using equations (2.8) and (2.9), where the values of $J(F, N_d, N_d)$ are taken from an input file. This function has been evaluated beforehand at discrete values of F using the NEGF model discussed in [6]. However, since these calculations are computationally intensive[1], the number of evaluated points is limited and interpolation algorithms are required for accurate results. Linear and cubic interpolation algorithms as well as cubic splines have been implemented and compared in order to obtain more accurate values in between the discrete points in F. Their properties and relative performance is discussed further in appendix A.

The inner loop is broken if either of two criteria are fulfilled. The first criteria is if the electric fields has reached a stable configuration. This is determined by checking if the maximum relative change in electric field strength within a period exceeds some predefined value. The second criteria is if the elapsed time reaches some maximum time t_{max}. This condition is introduced as some field configurations can oscillate, and thus never reach a stable configuration.

The inner loop is enclosed by an outer loop, as shown in figure 3.1. When the inner loop ends, any data of interest is written to appropriate output files. If the final bias has not been reached, the total bias is now increased with some delta bias ΔU. The final configuration of electric fields, from the inner loop, is preserved for the next bias. However, the field across each period is increased by $\frac{\Delta U}{d}$ in order to satisfy equation (2.3). Finally, the time is reset to zero before repeating the inner loop.

[1] The average time of a single simulation was about a week, using a CPU with 6 cores and 12 threads.

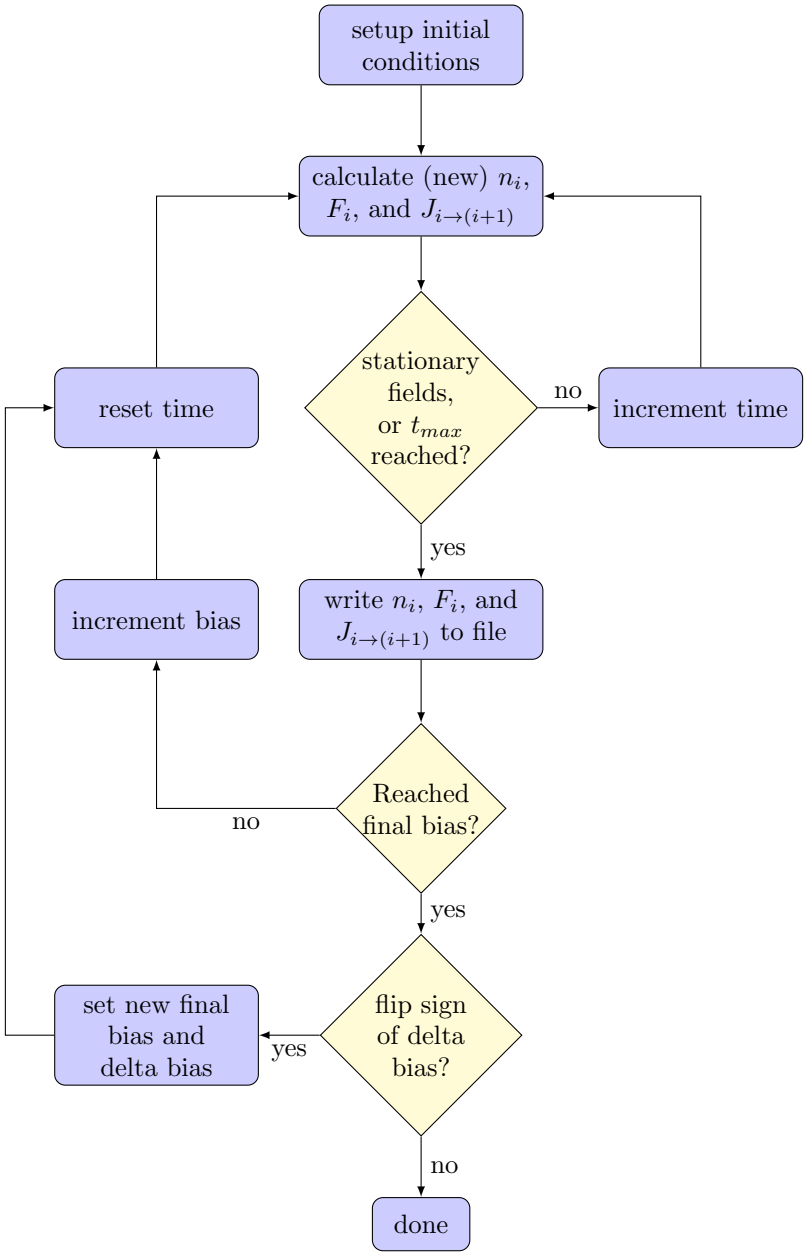

Figure 3.1: Flowchart of the EFD program. n_i denotes the two dimensional electron density in well i, F_i denotes the average electric field strength across period $i+1$, $J_{i\to(i+1)}$ denotes the current through period $i+1$, and t_{max} denotes the maximum simulated time for a single bias. Note that the *flip sign of delta bias* will at most yield yes once. For a more detailed description see section 3.

In order to more easily investigate particular configurations of EFDs, a feature is introduced that reverses the sweep direction if a flag is set to true. When the final bias is reached, this feature flips the sign of ΔU, and a sets new final bias. The time is also reset to zero, and the program returns to the inner loop. Further, another feature for investigating the time dependence of EFDs has been implemented. If a flag is set to true, data is periodically written to a different set of data files during the time evolution of the final bias point. Additionally, an increased maximum time for the final bias point can be specified.

In order to simulate the circuit used in experiments, the model needs to be altered such that the bias across the QCL can vary in time. The total bias across both the resistor and the QCL is now the constant quantity. Another set of integration methods have been implemented, that are used if the resistance defined in the input file is greater than zero.

The first approach still numerically integrates the electron densities, using equation (2.1). However, U is now also numerically integrated using equation (2.16), where J is given by the current through the resistor from equation (2.10). Just as before the electric fields are computed using equations (2.2) and (2.3).

The second approach numerically integrates all the electric fields using equation (2.19). However, now J is given by equation (2.10). New electron densities are computed using equation (2.6). Finally, equation (2.3) is used to calculate a new value of U.

Both theoretical approaches were implemented to provide a way to validate the results. However, the second approach, which integrates the electric fields, was used for all the presented results. This approach was chosen due to marginally shorter computation time, as well as being sleeker due to identical differential equations. Further, a timestep of $h = 1\,\mathrm{ps}$ was used in all the presented results, and was occasionally halved in order to confirm that it was sufficiently small.

The simulation of a single bias point can take up to five minutes to perform on a modern computer, using a single thread. Sweeping over a large number of bias points can take up to a few hours, heavily depending on the stability of the EFDs.

4 Bias Controlled Conditions

The QCL structure referred to as V843 features a phonon-photon-phonon design [8]. The energy of the lower band edge of the conduction band as well as the Wannier-Stark states under operation bias can be seen in figure 4.1 a). An longitudinal optical phonon resonance is used for extracting electrons from the green lower laser state, to the purple extraction state. From there, the electrons tunnel into the yellow injection state via resonant tunnelling, and then, through another longitudinal optical phonon resonance, relaxes into the blue upper laser state. After relaxation via stimulated emission into the next lower laser state, the process is repeated in the next QCL period. As this

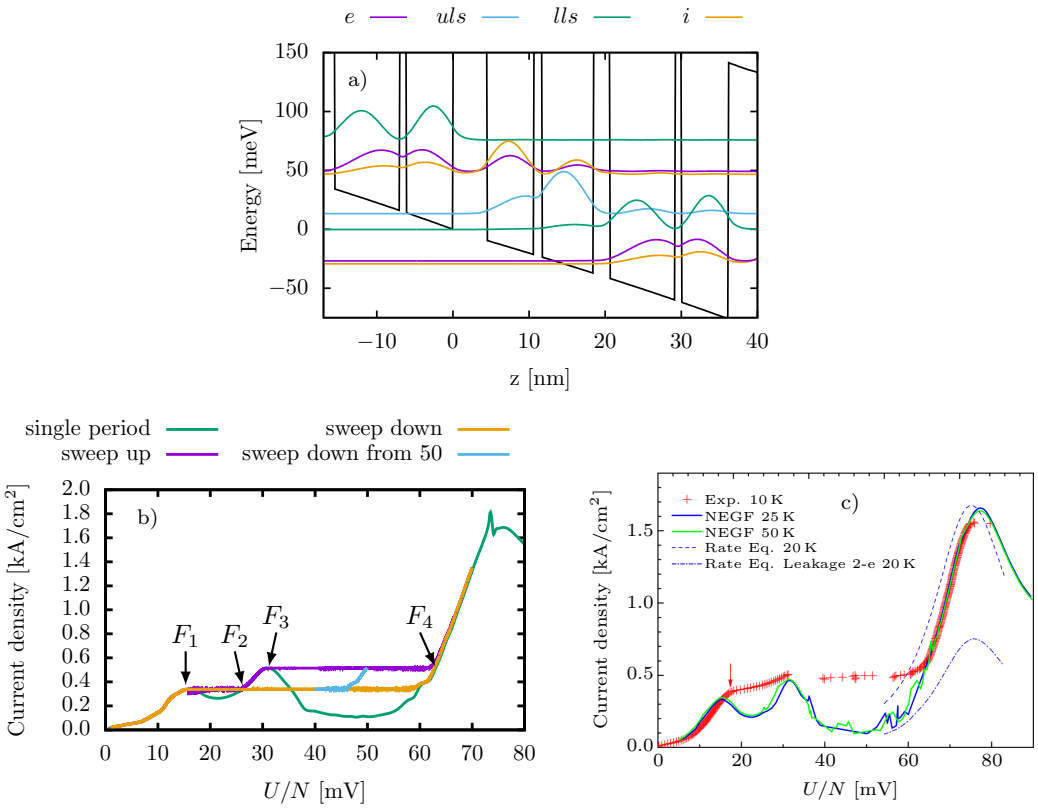

Figure 4.1: a) The solid black line is the energy of conduction band edge as a function of growth direction, z, at the designed external bias. Coloured lines are the absolute square of the most important Wannier-Stark states, at their respective energies. i is the injection state, uls the upper laser state, lls the lower laser state, and e is the extraction state. b) Simulated current density as a function of bias for the V843 sample. The green line displays data from a NEGF simulation with a uniform bias, which shows how a single period behaves. The other lines are simulations of EFD, where purple is a sweep up, and yellow is a sweep down. The blue line is a sweep down which started in a sweep up configuration at 50 mV per period. The EFD simulations was performed using Ohmic boundary conditions with $\sigma/A = 50\,\mathrm{A\,mV^{-1}cm^{-2}}$, a temperature of 50 K, and $N = 276$ periods. c) Experimental and simulated current density as a function of average bias per period. Taken from reference [8] with permission from the authors.

structure was grown with 276 periods, all simulations of EFDs were performed with $N = 276$ unless otherwise stated.

The simulated current as a function of bias for the V843 structure at 50 K is shown in figure 4.1 b). A temperature of 50 K was chosen because the NEGF program experiences difficulties to converge, with respect to the current, at very low temperatures. The green line is the current for a single period, obtained via NEGF simulations, and has three major peaks. Note that the sharp peak at 72 mV per period is an artefact of the simulation. It arises because the potential energy difference for an electron, when displaced one period, is exactly two times the phonon energy. The other lines are obtained from simulations of EFDs. The purple line shows the current during a sweep up, e.g. when the bias is slowly increased. The plateau following each peak is a clear sign of the formation of EFDs. The yellow line is the current during a sweep down, which also shows a wide plateau, indicating domain formation. The fact that the sweep down follows a different path than the sweep up is usually referred to as a hysteresis loop. This has been observed for different QCL structures, both experimentally [9] and in similar simulations [10].

Figure 4.1 c) shows experimental data for the same structure in red plus signs. It also shows the result of NEGF simulations using an older version of the same program as used to obtain the green line in figure 4.1 b). As can be seen, the measured current at the main plateau, between 31 mV and 63 mV, are in excellent agreement with the simulated sweep up with EFDs in figure 4.1 b). The first plateau on the other hand, is not observed in experiments. Here, the current is continuously increased for the bias range between 16 mV to 24 mV. Additionally, no observation of EFDs where made within this region in [11]. One possible explanation for this is that electron-electron scattering is not included in the NEGF model [6]. Early calculations suggest that the impact of electron-electron scattering is particularly strong in this region, indicating that this minimum may not exist [12].

Figures 4.2 a) and 4.2 b) show the local electric field strength, resolved in period index, for the sweep up and sweep down from figure 4.1 b), respectively. During the sweep up, there are two bias regions where EFDs can be observed. The first one occurs between 16 mV and 24 mV average bias per period. The electric field strength within the first EFD is shown as F_1 in figure 4.1 b). As no configuration of EFDs can exist for an extended period of time if the domains have a different current density, the second EFD will have an electric field of F_2. In figure 4.1 b) it is located at the rising side of the second current peak, with a current density equal to the peak value of the first peak.

The second region with EFD occur between 31 mV and 63 mV average bias per period. For the same reason as argued above, the electric field strength of the two EFDs within this region are F_3 and F_4 as shown in figure 4.1 b). Similarly to the first plateau, the low EFD is at a current peak and the high EFD is at the rising side of the next current peak. The sweep down shows a distinctly different behaviour compared to the sweep up. Only a single region of domain formation is observed between 16 mV and 60 mV average bias per period. The two EFDs within this region correspond to F_1 and a value slightly below F_4.

4.1 Oscillating Electric Field Domains

During the simulation of the sweep up, shown in figure 4.2 a), no stable configurations of the electric fields could be observed between 16 mV and 24 mV. When looking more carefully at the current during the sweep up in figure 4.1 b), and on the boundary between the two domains in figure 4.2 a), they are both very rough. An explanation for this is found when looking at the time dependence of the EFDs, which is plotted in figure 4.3 a). This figure clearly shows how the position of the boundary between the EFDs, which contain the charge accumulation, is oscillating in time. As shown in figure 3.1, the fields are evolved in time until a convergence requirement is fulfilled, or a maximum time is reached. Hence, for the oscillating EFDs, the currents and fields that are presented in 4.1 b) and 4.2 a), are the values that was present at the maximum time.

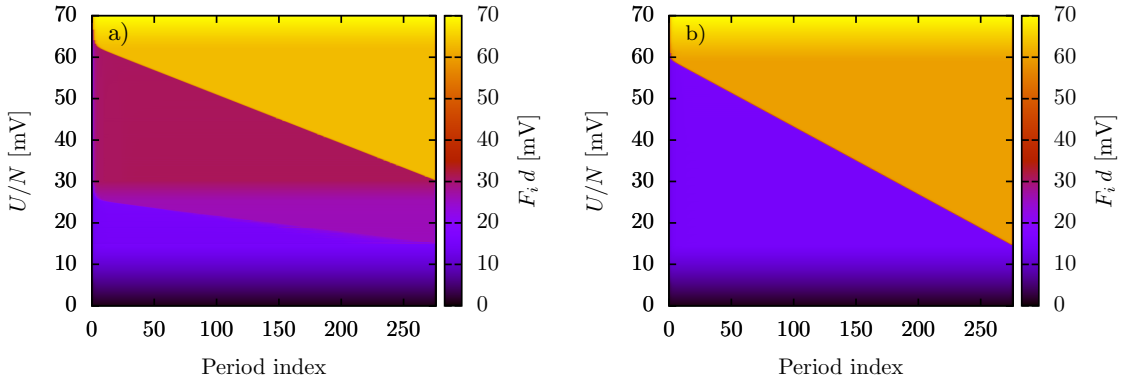

Figure 4.2: Local bias drop per period resolved in period index and the average bias per period for a) sweep up, b) sweep down. Parameters as in figure 4.1 b). For the oscillating domains, the electric field strengths are taken at an arbitrary time.

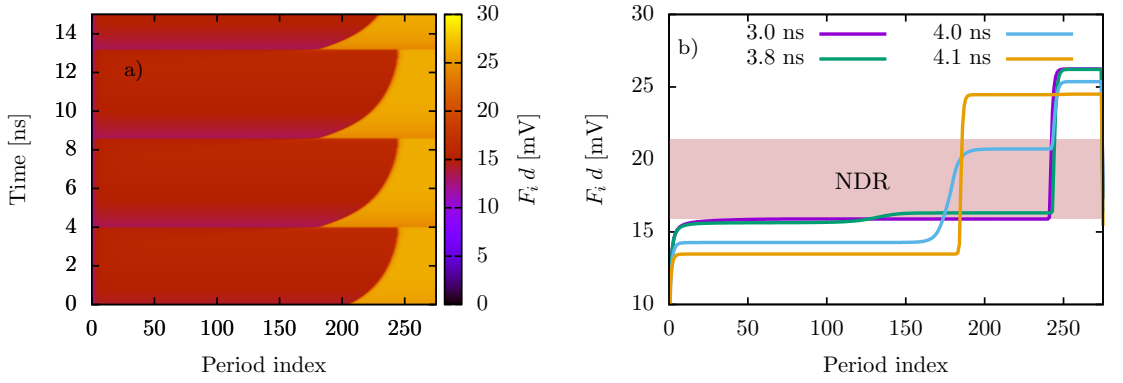

Figure 4.3: a) Time dependence of the EFDs during a sweep up at an average bias of 17 mV per period. Other parameters as in figure 4.1 b). b) Electric field strength as a function of period index at some key times for the same conditions as in a. The region of NDR is highlighted.

Figure 4.3 b) is a two dimensional plot at some key times for the same data as figure 4.3 a). The NDR region between the first two peaks in figure 4.1 b), is indicated by the highlighted region in figure 4.3 b). At 3 ns we have two distinct EFDs, where the first domain is exactly at the first current peak. Slightly later at 3.8 ns a small number of electrons has accumulated around period number 130, which can be seen by the increase in electric field strength there. Now the first EFD has been split into two, where the first one is still at the first current peak, but the second one has been pushed into the NDR region. Because of the NDR region the middle EFD will now conduct worse than both the first and the last EFD. A direct consequence of this is that the first, small, charge accumulation will accumulate more electrons, while the second charge accumulation will be depleted. This is exactly the effect seen happening in the line corresponding to 4 ns. Finally at 4.1 ns the first charge accumulation has completely replaced the other one, and we once again have two EFDs. The boundary between the two will continue to travel until this process is repeated. It is noteworthy how quickly this sequence of events occur, a full period is slightly longer than 4 ns while the process of replacing the existing charge accumulation happened in about 0.3 ns.

The next logical question is why do these EFDs oscillate, while the EFDs at the main plateau in figure 4.2 do not? To explain this we must first note that the electric field strength goes down rapidly near the contacts, where the injection contact is next to period 0 and extraction contact is next to period 276. This is an indication that the contacts conduct much better than the QCL itself. Electrons accumulate near the injection barrier, and the electron density is brought lower than the doping density near the extraction barrier, which reduces the current at each of the contacts.

Now postulate that the boundary between the two domains is travelling. When the boundary is travelling, the electric field strength in both EFDs is slowly increased to keep the total bias constant. At some point, the first EFD will reach the top of the first current peak, and subsequently the NDR region behind it. When this happens, the first domain will have a lower conductance than some point near the injection barrier on the left side in figure 4.3 b), as the field strength is lower here. This will cause electrons to accumulate there which decreases the electric field strength on the left of the accumulation, and increases on the right. As increasing the field strength causes a lower conductance of the domain, this will amplify the rate at which electrons are accumulated. Hence, the behaviour we are observing is obtained. It is noteworthy that the exact same argument holds for explaining why EFDs are formed during a sweep up, by considering a uniform electric field

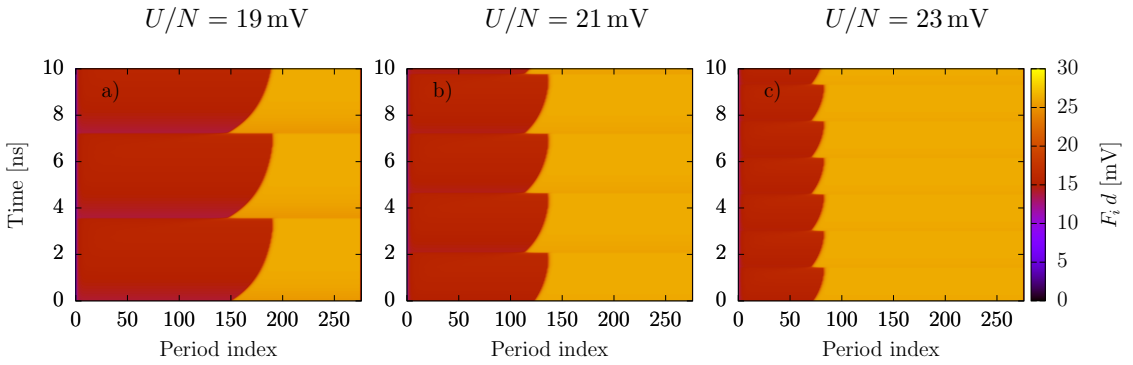

Figure 4.4: Electric field strength as a function of period index and time for different average bias per period. a) 19 mV/per, b) 21 mV/per, and c) 23 mV/per. Other parameters as in figure 4.1 b)

which is slowly increased.

The final question we need to answer is: Why do the boundary between the EFDs travel? It has been shown that, for a continuous charge distribution, EFDs cannot be stationary [13]. Hence, the steady domains are a feature of the discrete periods of the QCL, and can only be seen when essentially all of the charge accumulation is within a single period. Consider the case where the first EFD is at the first current peak, and the second EFD is at the equivalent current density at the rising side of the second peak. The periods of the QCL which contain the charge accumulation will have some intermediate field strength, which corresponds to a current within the valley between the two peaks. From equation (2.8) one can see that the current through a period also has a term proportional to the number of electrons within that period. Further, for a steady configuration a constant current density throughout the QCL is required. This requirement implies that a shallow minimum between the current peaks, or a large total charge accumulation, causes the charge accumulation to spread out over a larger number of periods. As argued in [4], a large total charge accumulation indicates a large difference in electric field strength. Hence, instability can be attributed to a shallow minimum, as well as a large separation in bias between the current peaks.

Figure 4.4 shows plots of the electric field strength as a function of period index and time. These plots are similar to 4.3 a), with the difference that they are taken at a higher total bias. The average bias per period in figure 4.4 from left to right are, 19 mV/per, 21 mV/per, and 23 mV/per. As expected, the high EFD extends over a larger number of periods at a greater bias. Another noticeable difference is the more rapid oscillations at higher biases. This can be explained by considering the distance which the charge accumulation has to travel before a new one develop. The velocity of the charge accumulation is by no means constant, as can be seen by the changing slope of the boundary in figures 4.3 a) and 4.4. However, the much reduced distance it has to travel is sufficient to reduce the period of the oscillations.

4.2 Triple Electric Field Domains

The blue line in figure 4.1 b) was obtained by sweeping up to $U/N = 50\,\mathrm{mV}$ and subsequently reversing the sweep direction. Figure 4.5 a) shows the electric field strength as a function of period index and U/N during this sweep down. The structure starts in a sweep up configuration of EFDs, and the individual field strengths are initially reduced during the sweep down. This also reduces the current, until a current equal to that of the first peak in figure 4.1 b) is reached. At this point, periods with a bias at the second current peak start to transition to a bias at the first current peak. This creates a configuration with three EFDs, which allows the structure to make a transition into a sweep down configuration. The sweep down configuration is reached at $U/N = 42\,\mathrm{mV}$ figure 4.5 a).

Figure 4.5 b) shows the time resolved EFDs for the particular configuration in figure 4.5 a) with $U/N = 43\,\mathrm{mV}$. As the two lower EFDs have the same field strength as those in figure 4.3, they are also oscillating in this scenario. The period of the oscillations are much shorter than that in figure 4.3 a), as the charge accumulations have a significantly shorter distance to travel. In fact, the period is very similar that that in figure 4.4 c), where the charge accumulation front has a very similar distance to travel. This indicates that the high EFD has little to no impact on the oscillations.

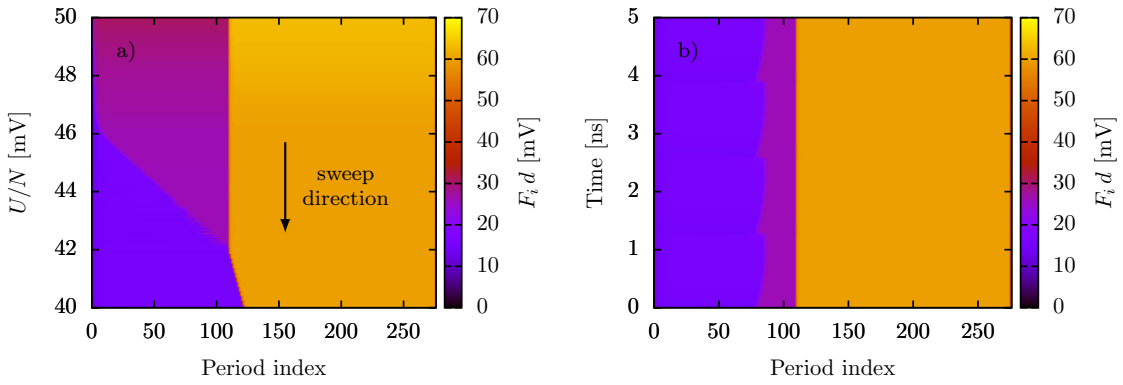

Figure 4.5: a) Electric field strength resolved in period index for a sweep down that started in a sweep up configuration at $U/N = 50\,\mathrm{mV}$. The current density during this sweep down is shown with the blue line in figure 4.1 b). b) Electric field strength as a function of time and period index. $U/N = 43\,\mathrm{mV}$, and the particular configuration of EFDs is the same as in a).

5 Simulations Including the Experimental Circuit

Including the experimental circuit in the simulations changes the allowed combinations of U and J. One of the consequences is that it changes the dynamics of the EFDs. When the experimental circuit is considered, a so called load line is introduced. The load line is the combinations of U and J that fulfil equation (2.10), and can be seen in figure 5.1 b). Any changes to J will move parallel to the load line in this figure, for a given U_0. In contrast, with a fixed bias, J will always move vertically. The current through the QCL can deviate from J however only for a limited time, as this cause electron accumulation or depletion.

5.1 Comparison with Controlled Bias

The main plateau in the current profile of the V843 sample is shown in figure 5.1, where 5.1 a) is with a constant bias, and 5.1 b) is with a load line using the same number of bias points. The spacing between the bias points, ΔU, is larger for 5.1 a) compared to 4.1 b). This causes the roughness of the green line in figure 5.1 a). When ΔU is large, the boundary between the EFDs move multiple periods at a time. When this happens, J move down vertically with a constant bias, as seen in figure 5.1 a). However, when a load line is used J move parallel with it, as seen in figure 5.1 b).

The load line has a significant impact on the dynamics of the EFDs. This becomes evident when the oscillations between the first two current peaks are compared with constant bias and with a load line. Figure 5.2 a) shows the oscillations with an average bias of 17 mV/period over 25 ns. In figure 5.2 a), similar oscillations with a load line are shown, where the bias was chosen such that the charge accumulations have to travel approximately the same distance.

Two significant differences are immediately noticeable when comparing figure 5.2 a) and 5.2 b). The first one is the much longer periods with the load line. The velocity of the electron accumulation is lower when the load line is used, primarily for larger widths of the high EFD. The second difference is that the electric field strength within the EFDs changes much more with a constant bias. With a constant bias, the field strengths are forced to be reduced when the width of the high EFD is increased. However, with a load line this is no longer the case. Instead, the bias across the QCL, U, is increased as can be seen in figure 5.3 a). When U is increased, the bias, and hence also the

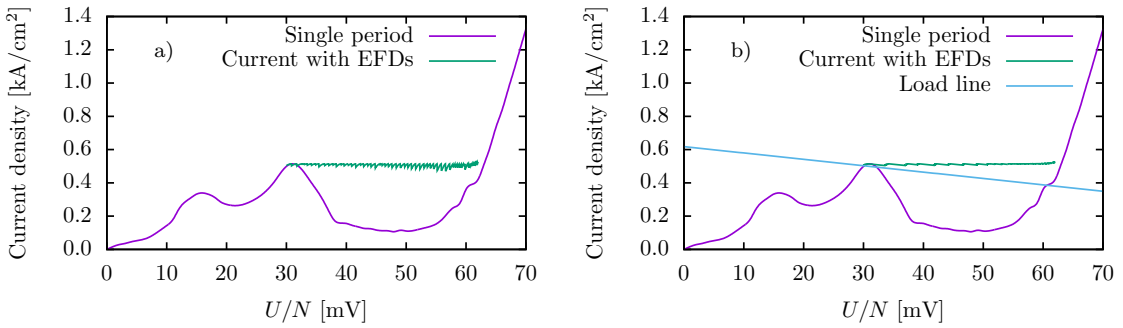

Figure 5.1: A bias sweep up, covering the main plateau of the V843 QCL at 50K, with a conductance of $\sigma/A = 50\,\mathrm{A\,mV^{-1}cm^{-2}}$. a) Constant bias. b) Load line with a resistance of 50 Ω, as is typically used in experiments [14].

current through the resistor is reduced. Therefore, the current is still reduced with the load line, which is shown in figure 5.3 b), but not as much as with a constant bias.

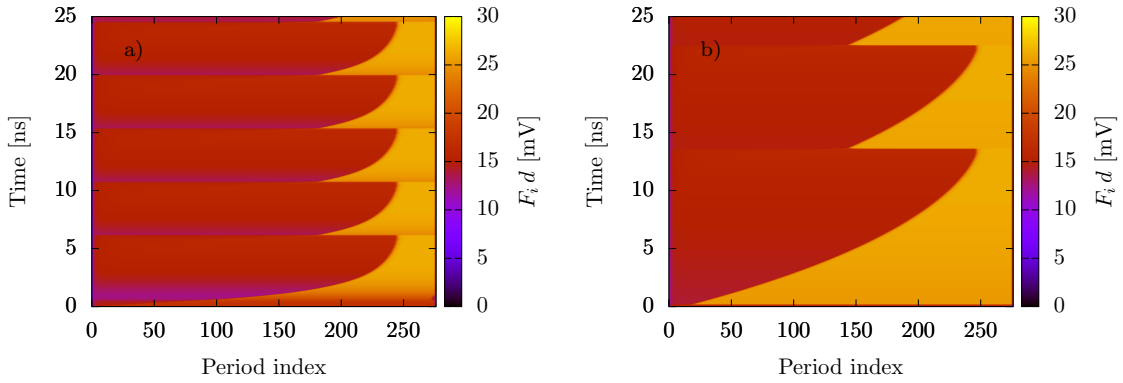

Figure 5.2: The local electric field strength is shown as a function of time and period index. a) Using a constant bias of 17 mV per period. b) Using a load line with $U_0 = 29.1\,\mathrm{V}$, and a resistance of $50\,\Omega$.

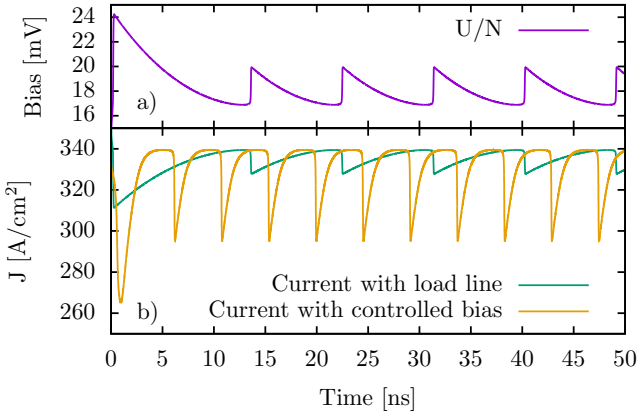

Figure 5.3: a) The average bias as a function of time, using a load line with $U_0 = 29.1\,\mathrm{V}$, and a resistance of $50\,\Omega$. Data were taken from the same simulation as figure 5.2 b). b) The green line shows the total current density as a function of time, for the same simulation as a). The yellow line shows the total current as a function of time, using a constant bias of 17 mV per period. Data were taken from the same simulations as in figure 5.2

5.2 Charge Accumulations

The regions of electron accumulation and depletion are essential for the behaviour of EFDs. As shown in [13], continuous charge accumulations cannot be stationary. Stationary EFDs must therefore have essentially a single period which contains the charge accumulation. Figure 5.4 compares the accumulation front between a stationary domain at the main plateau and the travelling fronts at the first plateau. For the oscillating EFDs the charge accumulation travels between discrete modules of the QCL. When it travels, the difference in density between the two most populated modules will vary. The time used for figure 5.4 b) was chosen such that the difference between the density in the two most populated modules where as large as possible in order to show how narrow the accumulation front can become during these oscillations.

The electron accumulation for the stationary domains do indeed contain a majority of the charges within a single module of the QCL. However, a significant accumulation can still be observed in another one or two modules. The electric field domains at the main plateau of the V843 QCL have been directly imaged using scanning voltage microscopy [11], where all of the accumulated electrons was seen in a single period of the QCL. However, when looking back at our model in section 2 it becomes apparent that this is not allowed. The field within a period is given by $F_i = F_{i-1} + \frac{e}{\varepsilon}(n_i - N_d)$. If all the accumulated electrons were placed within a single period, that period will have the same electric field strength as the high EFD. With the additional electron density, equation (2.8) results in a much greater current density compared to the high EFD. This model clearly cannot form stable domains with all of the accumulated electrons within a single period.

The model that is used for the simulations was initially developed for superlattices. However, what it really describes is the transport of electrons between discrete points in space, with a predefined current density as a function of bias between the individual points. Due to the periodicity of the QCL, it doesn't matter where within each period of the QCL the electrons accumulate, as long as the accumulation has essentially the same shape for each QCL module. This assumption is very reasonable within an EFD, as each of the modules experience identical electric field strengths

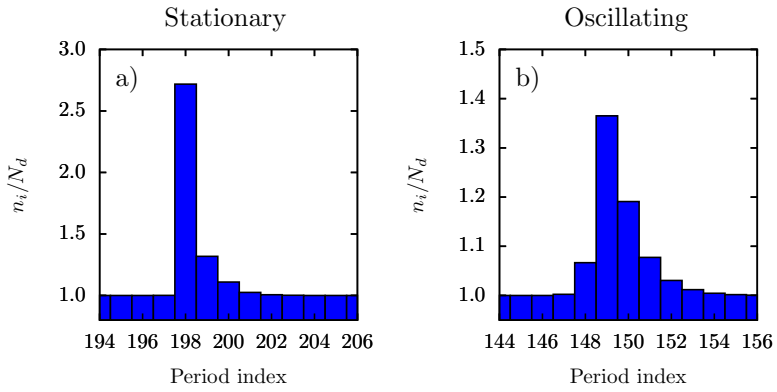

Figure 5.4: Relative electron density as a function of period index in the V843 QCL at 50 K. Simulated with a resistance of 50 Ω in series, and without an external capacitance. a) During a sweep up of structure V843 at an average bias of 39.8 mV per period. b) During the oscillations shown in figure 5.2 b), with an average bias of 17 mV per period.

and the electron density is equal to the doping density. However, the electrons do not necessarily accumulate at the same position in the module for the different EFD. This would potentially change the effective width of the modules in the transition region between the EFDs.

In order to investigate weather the above argument could be a source of error, the electron density as a function of growth direction from the NEGF simulations was investigated. The spatially resolved electron densities within the two domains at the first and second plateaus are compared in figure 5.5 a) and 5.5 b), respectively. The electrons accumulate at essentially the same point for the two domains at the first plateau. However, at the second plateau the electron densities is shifted down-stream for the high EFD. In the simple scenario of a single transition module, the effective width of this module would be increased. This would alter the average current density through the transition period depending on the shape of the spatially resolved current density.

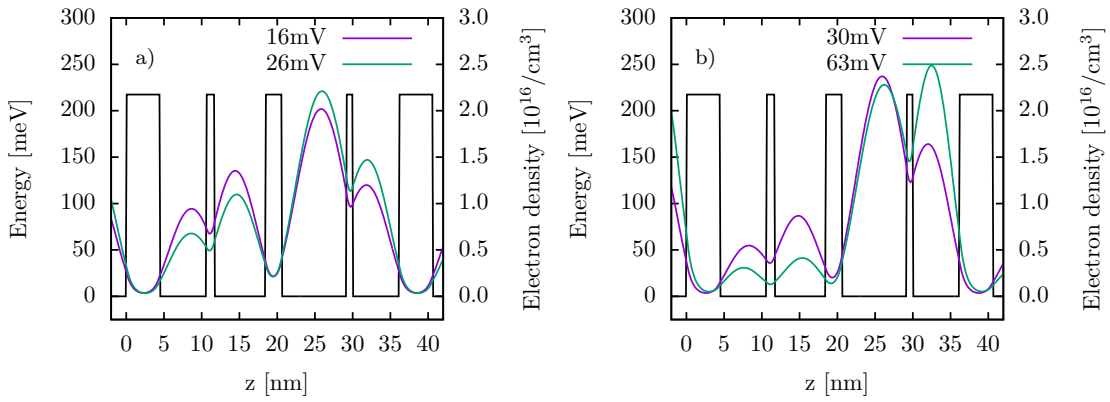

Figure 5.5: The electron densities, resolved within a period of the QCL, obtained from the NEGF simulations. For 16 mV and 26 mV in a), approximately equal to F_1 and F_2 in figure 4.1 b), corresponding to the electric field strengths within the EFDs at the first plateau. For 30 mV and 63 mV in b), which are approximately equal to F_3 and F_4 in figure 4.1 b), and correspond to the electric field strengths within the EFDs at the main plateau.

5.3 Reduced Contact Conductance

There has been evidence of current oscillations in the V843 QCL within the main plateau of the current profile at 10 K [14]. However, this is not observed in our simulations at 50 K, as discussed in section 4. A significant difference at very low temperatures is that carriers might get trapped at the donor atoms [15]. This effect would significantly impair the conductance of the structure. In an attempt to imitate this behaviour, the conductance of the injection barrier was significantly reduced. A number of different conductances for the injection barrier were tested, of which three are presented in this section. In all cases, the conductance of the extraction barrier was kept unchanged, such that the current through the final barrier is greater than that of a QCL module, with N_d electrons, for any given electric field strength.

5.3.1 Moderate Conductance

Several noticeable differences immediately arise due to a reduced contact conductance, which is shown in figure 5.6 a). The contact conductance is now below the current for a single QCL period for all three peaks. The green line in this figure shows the current with EFDs during a simulated sweep up. As can be seen, the current with EFDs can go above the line that corresponds to the contact conductance.The first couple of periods are depleted which increases the electric field strength across the injection barrier, and thus also the current. However, the top of the peaks can no longer be resolved during the sweep up. Clearly there is a limit to the depletion of the initial modules, before it becomes unstable.

The main plateau can no longer be seen at all in figure 5.6 a). In a single jump, the structure moves from a uniform field at the second peak to a uniform field at the third peak. This is shown by the dashed part of the green line that is parallel to the yellow load line. The fact that the current is

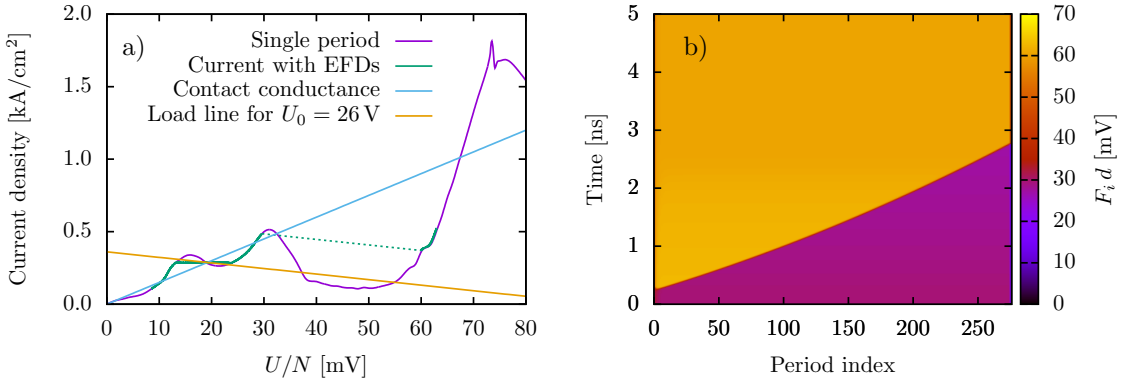

Figure 5.6: a) The purple line is the current as a function of bias for a single period of the QCL from NEGF simulations. The green line is the current density during a bias sweep up with the EFD program at 50 K, where the dashed region indicates where a large jump in bias takes place. The blue line shows the conductance of the injection barrier, with $\sigma/A = 15\,\mathrm{A\,mV^{-1}cm^{-2}}$. The yellow line is the load line with a resistance of 50 Ω, here shown for $U_0 = 26$ V. b) The local electric field strength resolved in period index and time, for $U_0 = 43.2$ V. At this bias, the structure transitions from a uniform field at the second current peak to a uniform field at the third current peak. Other parameters as in a).

above the contact conductance immediately before the jump tells us that there is now an increased electric field strength near the injection barrier. In section 4.1 it was argued that: since the electric field strength is lower near the injection barrier, some point near the injection barrier will conduct better than the EFD, when the EFD reaches the NDR region. This argument clearly no longer holds for the scenario in figure 5.6. Since the field strength is greater near the injection barrier, a number of the QCL periods are inside the NDR region even before the peak is reached. Eventually, the depletion region detaches from the injection barrier, and travels through the QCL, as shown in figure 5.6 b). It is most likely possible to construct stable configurations where the plateau is expected, but they do not get a chance to form under these circumstances.

With the reduced conductance for the injection barrier, shown in figure 5.6 a), the oscillations at the first plateau are significantly different from those seen so far. Figure 5.7 shows the average bias as a function of time, and the local electric field as a function of period index and time, for three different biases at the first plateau. The current as a function of time is here ignored as it is a perfect mirror of the bias, as shown in figure 5.3. The bias as a function of time can have a significantly different shape with relatively small variations in bias.

For all three biases in figure 5.7, a high field domain is formed near the injection barrier, which subsequently detaches and travels through the structure. It can also be seen that the accumulation front, trailing the high EFD, seen in orange in figure 5.7, has a greater velocity compared to the depletion front. This causes the width of the high field domain to be reduced in time and, at lower biases, it disappears entirely before reaching the extraction barrier. Further, all significant changes to the rate of change of the bias can be related to some event in the corresponding plot of the fields. For all scenarios the bias is rapidly increasing as the first high field domain is formed. The peak is reached when the high field domain detaches.

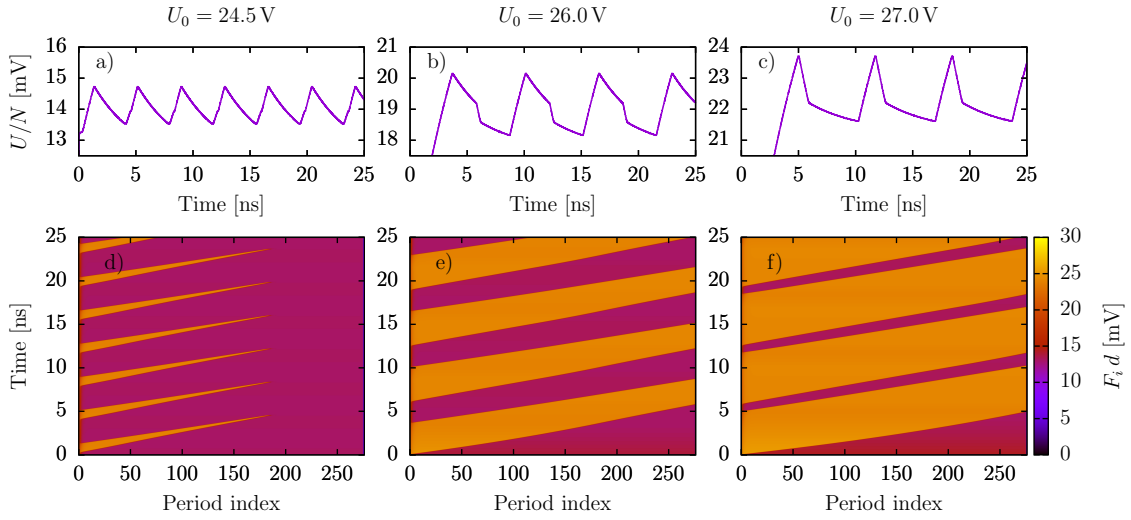

Figure 5.7: The top row shows U/N as a function of time, for a) $U_0 = 24.5\,\mathrm{V}$, b) $U_0 = 26.0\,\mathrm{V}$, and c) $U_0 = 27.0\,\mathrm{V}$. The bottom row shows the electric field strength as a function of period index and time, for d) $U_0 = 24.5\,\mathrm{V}$, e) $U_0 = 26.0\,\mathrm{V}$, and f) $U_0 = 27.0\,\mathrm{V}$. Other parameters are defined in figure 5.6 a).

For $U_0 = 24.5\,\mathrm{V}$, figure 5.7 a), the minimum is reached when the next high field domain is formed, at which point the bias starts to increase again. Subsequently the first high field domain disappears entirely, which causes the bias to increase more rapidly than before. Finally, the next peak is reached when the second high field domain detaches.

At $U_0 = 26.0\,\mathrm{V}$, figure 5.7 b), the bias is reduced more slowly when the first high field domain detaches. This is followed by a much more rapid reduction of the bias when the high field domain reaches the extraction barrier. Shortly after, a second high field domain is formed at the injection barrier, and the bias is now slowly decreasing. The next rapid increase occurs when the first high field domain disappears entirely.

At the even greater bias of $U_0 = 27.0\,\mathrm{V}$, figure 5.7 c), a very sharper peak is present at 5 ns. A closer look at the plot of the electric fields shows that the first high field domain reaches the extraction barrier and detaches from the injection barrier at the same time. This explains the sudden transition from a rapid increase in bias to a rapid decrease in bias. The rapid decrease ends when a second high field domain is formed. The bias is then slowly decreasing until the first high field domain disappears, at which point the bias is once again increased rapidly.

5.3.2 Low Conductance

By further reducing the injection barrier conductance, the second current peak can barely be resolved at all during a sweep up, as can be seen in figure 5.8 a). The conductance of the injection barrier is now lower than that of a single period of the QCL until some point within the second NDR region. At this reduced current, once again some stable configurations within the main plateau can be observed. However, large jumps still take place which are indicated by the dashed parts of the green line in figure 5.8 a). When these sudden bias jumps occur, the new configuration can take

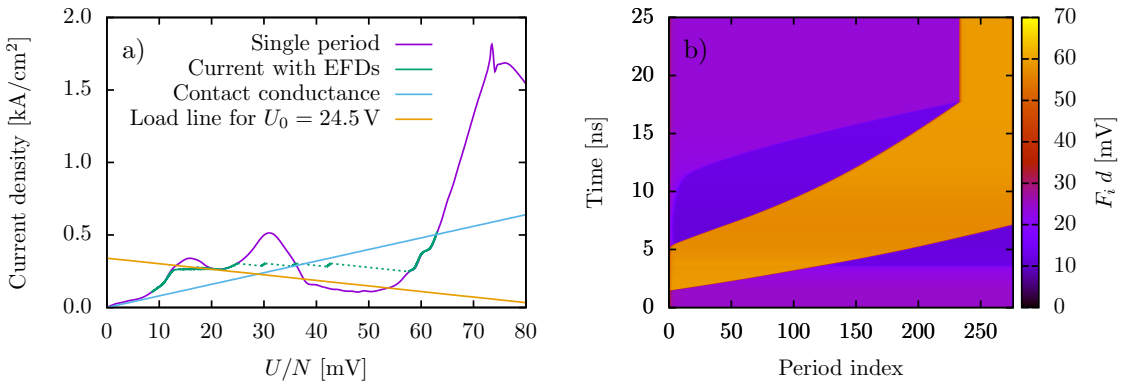

Figure 5.8: The purple line is the current as a function of bias for a single period of the QCL from NEGF simulations. The green line is the current density during a bias sweep up with the EFD program at 50 K, where the dashed regions indicate where large jumps in bias take place. The blue line shows the conductance of the injection barrier, with $\sigma/A = 8\,\mathrm{A\,mV^{-1}cm^{-2}}$. The yellow line is the load line with a resistance of $50\,\Omega$, here shown for $U_0 = 24.5\,\mathrm{V}$. b) The local electric field strength resolved in period index and time for $U_0 = 43.2\,\mathrm{V}$. At this bias, the structure stabilises in a domain state after a long jump in bias. Other parameters as in a).

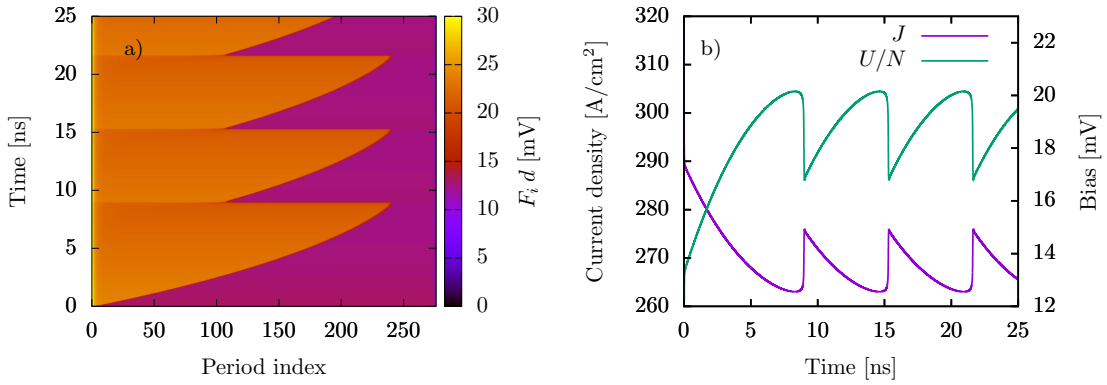

Figure 5.9: a) U/N as a function of time for $U_0 = 24.5$. b) The electric field strength as a function of period index and time for $U_0 = 24.5\,\mathrm{V}$. Other parameters as defined in figure 5.8 a).

close to 20 ns to stabilise, as shown in figure 5.8 b). The main difference compared to the figure 5.6 b), is that when a high field domain is formed near the injection barrier, it now detaches and travels to the extraction barrier, where it becomes stable. It can also be seen that the electric field strength within the EFDs is reduced as the depletion front travels. At some point the low EFD reaches the minimum between the first two peaks, at which point it suddenly jumps down to a bias below the first peak. Subsequent to the detachment of the accumulation front from the injection barrier, another depletion front is formed and detaches after about 10 ns. This depletion front travels significantly faster than the accumulation front, and also has a much smaller magnitude. This creates an intermediate EFD at the injection barrier, followed by a low EFD and a high EFD at the extraction barrier. Once the depletion front catches up with the accumulation front, the low EFD disappears and the accumulation front becomes stable.

Oscillations before the second current peak can still be observed, and are shown for one bias point in figure 5.9 b). The general shape of figure 5.9 a) is very similar to the oscillations discussed in section 4, with the difference that the high EFD is now near the injection barrier. This implies that it is now depletion fronts that are created and travel through the structure. The bias oscillations shown in figure 5.9 b) are, as expected, also very similar to those in figure 5.3 a) but they look as though they are mirrored along the x-axis. This is not surprising, because when the boundary between the EFDs jumps to the left, the total bias is now decreased instead of increased.

5.3.3 Very Low Conductance

By reducing the injection barrier conductance even further, oscillations can be observed in the bias region corresponding to the main plateau. However, as can be seen in figure 5.10, the second peak can no longer be resolved at all during a sweep up. The domains now have an electric field strength corresponding to a bias per period significantly below the first peak, and very far down at the third peak. This means that the current within the minimum is no longer far below that of the two domains, which causes a spread out accumulation or depletion fronts, and travelling domains.

The oscillations observed with this low contact conductance are similar to those observed in section 5.3.1. Looking at the local electric field strength in figure 5.11, it becomes apparent that

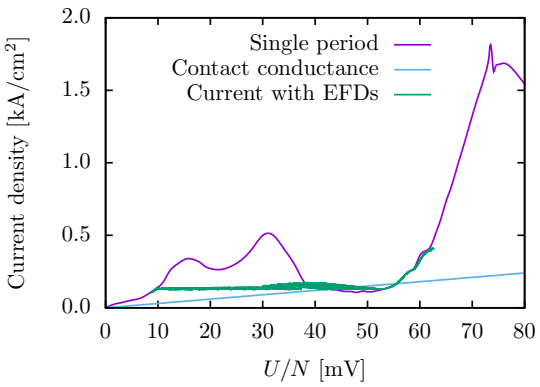

Figure 5.10: The purple line is the current as a function of bias for a single period of the QCL from NEGF simulations. The green line is the current density during a bias sweep up with the EFD program at 50 K. The blue line shows the conductance of the injection barrier, with $\sigma/A = 3\,\mathrm{A\,mV^{-1}cm^{-2}}$. The yellow line is the load line with a resistance of 50 Ω, here shown for $U_0 = 18\,\mathrm{V}$.

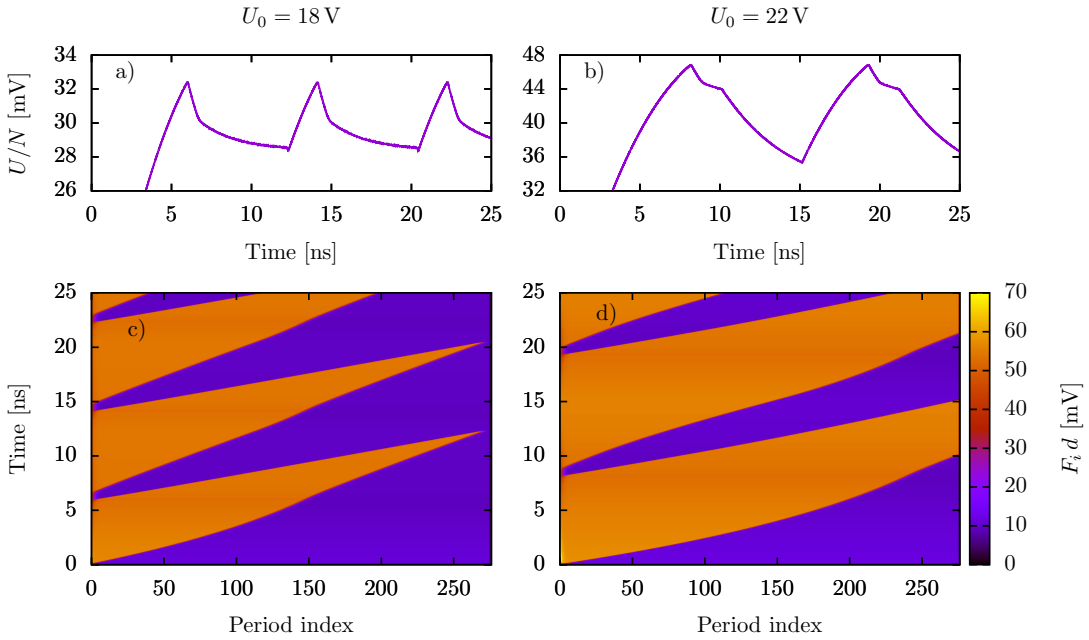

Figure 5.11: The top row shows the average bias per period across the QCL, U/N, as a function of time, for a) $U_0 = 18\,\mathrm{V}$, b) $U_0 = 22\,\mathrm{V}$. The bottom row shows the local electric field strength as a function of period index and time, for c) $U_0 = 18\,\mathrm{V}$, d) $U_0 = 22\,\mathrm{V}$. Other parameters are defined in figure 5.10.

the relative velocity between the depletion and accumulation fronts are noticeably different. When comparing to the average bias per period in the same figure, one can see that the bias is declining even when two depletion fronts and one accumulation front is present in the QCL. This indicates that the velocity of the accumulation front is greater than twice that of the depletion front at that time. However, the velocity of the depletion fronts are far from constant. Figures 5.11 c) and 5.11 d) show a significant decrease of the depletion front velocity near the extraction barrier.

Fairly similar oscillations can be observed when comparing figures 5.7 and 5.11. However, they take place at very different electric field strengths. Differences in the relative velocities of the accumulation and depletion fronts are significant and impacts the shape of the bias oscillations. Further, the curvature in between the sharp kinks of the bias oscillations reveals that the relative velocities also change during the oscillations. Something in the operating conditions changes the dynamics of the EFDs, and variations in the bias have little impact. On the other hand, changing the current would affect the spatial width of the accumulation and depletion fronts. As the width of these are crucial for stability, it would be reasonable that it would also affect the velocity of the fronts during oscillations.

In an attempt to change the current, with a maintained average bias per period, the injection barrier conductance was raised together with the total bias, U_0, such that the conductance and the load line intersect at a predefined bias per period. Three different injection barrier conductance and load line combinations are shown in figure 5.12, where the same type of dashes are used simultaneously.

Figure 5.13 shows the bias and local electric field strength as a function of time for the three combinations of injection barrier conductance and load line from figure 5.12. Its not too surprising

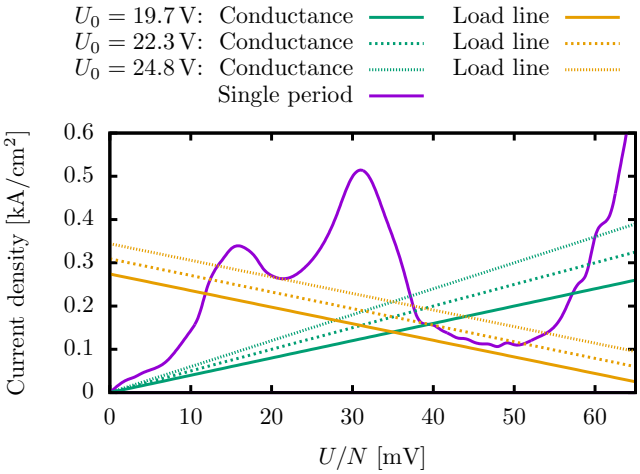

Figure 5.12: The purple line is the current as a function of bias for a single period of the QCL from NEGF simulations. The green lines show the current through the injection barrier for three different values of the conductance, used in the EFD program. The yellow lines are the load lines with a resistance of $50\,\Omega$, for $U_0 = 19.7\,\mathrm{V}$, $U_0 = 22.3\,\mathrm{V}$, and $U_0 = 24.8\,\mathrm{V}$, respectively. The corresponding injection barrier conductances are $\sigma/A = 4\,\mathrm{A\,mV^{-1}cm^{-2}}$, $\sigma/A = 5\,\mathrm{A\,mV^{-1}cm^{-2}}$, and $\sigma/A = 6\,\mathrm{A\,mV^{-1}cm^{-2}}$. The same type of dashes shows which conductance and load line was used simultaneously, and was chosen such that they intersect at 35 mV per period.

that the average bias per period was not kept constant, as the current depends not only the contact conductance and the load line, but also the current profile of the QCL has a vital role. However, the minimum bias during the oscillations was actually kept fairly constant, while the maximum bias increased significantly.

The local electric fields in figures 5.13 d), 5.13 e), and 5.13 f), reveals that the relative velocity between the accumulation and depletion fronts changes significantly for the different bias and contact conductance combinations. The high EFD is shrinking as it is travelling in figure 5.13 d), while it is growing in figure 5.13 f).

The current oscillations in figure 5.13 b) and 5.13 c) are very similar but with slightly different slopes. The rapid increase in bias ends when the first high EFD detaches from the injection barrier. A rapid decrease occurs when the first high EFD reaches the extraction barrier. The bias starts to increase again when a second high EFD is formed, and increases more rapidly when the first high EFD disappears entirely.

The oscillations in figure 5.13 a) are notably different from the other two. The secondary peaks in the oscillations are caused by the formation of a second high EFD before the first high EFD reaches the extraction barrier. When it does, the bias is reduced again. And high EFD disappears entirely, the bias is once again rapidly increasing.

We can here show that an identical configuration of EFDs evolve very differently in time, depending on various parameters. In the region around 5 ns in figure 5.13, the bias can both decrease and increase despite always having one depletion front followed by an accumulation front in the structure. Similarly, in the region shortly after 10 ns, both a rapid increase and a rapid decrease can be seen depending on the changed bias and conductance. For each set of parameters an accumulation front is followed by a depletion front in this region of time.

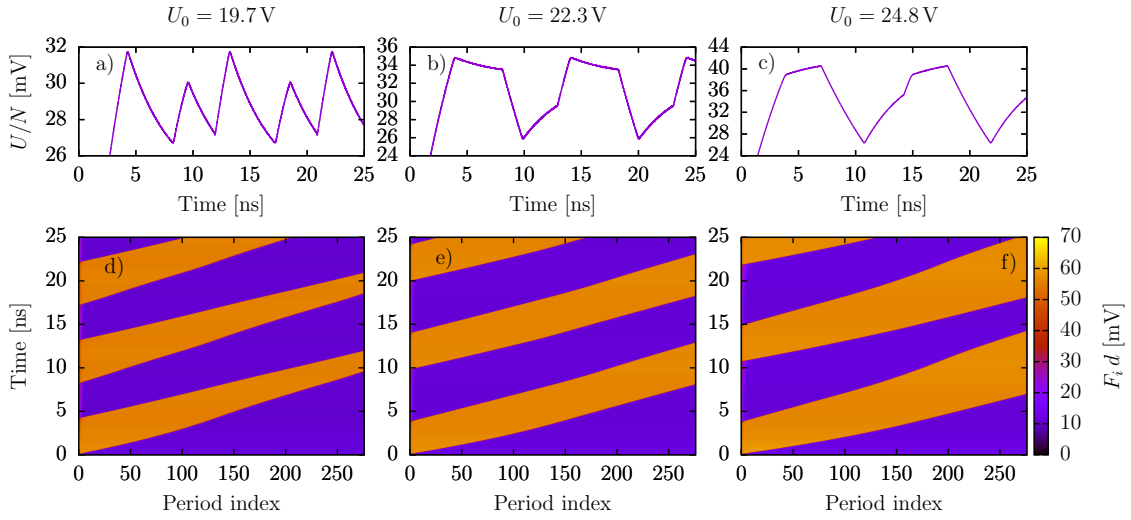

Figure 5.13: The top row shows the average bias per period across the QCL, U/N, as a function of time, and the bottom row shows the local electric field strength as a function of period index and time. The three columns uses the respective combinations of contact conductance and load line shown in figure 5.12, from left to right: $U_0 = 19.7\,\mathrm{V}$, $U_0 = 22.3\,\mathrm{V}$, and $U_0 = 24.8\,\mathrm{V}$.

5.3.4 Exponential Conductance

Since the QCL has a Schottky contact [8], simulations with an exponential conductance [16] for the injection barrier were also performed. Figure 5.14 shows the current during a sweep up for two different exponential conductances. The current during a bias sweep up with EFDs looks fairly similar to the previous section. Although, in figure 5.14 b) both the current and bias seems to oscillate with a larger magnitude, which is confirmed by figure 5.15 a) and b). An explanation for this is that the oscillations take place at a larger current. Figure 5.14 b) is very near stability, and a small increase in conductance yields a behaviour similar to figure 5.8 a). This is in good agreement with the observation in section 5.3.3, that the magnitude of the bias oscillations increases with a higher current.

Also the bias oscillations and fields in figure 5.15 look very similar to the oscillations observed with a linear conductance. Figure 5.15 a) is very similar to 5.11 b) with slightly altered velocities for the accumulation and depletion fronts, while figure 5.15 b) looks like something in between figure 5.13 b) and 5.13 b). The width of the different regions in figure 5.15 are also different however this depends to a large extent on the width of the EFDs, which in turn depends on the bias, U. Also in this scenario, each critical point of the bias plots can be related to either the creation or disappearance of an accumulation or a depletion front. No significant difference between exponential and linear injection barrier conductance were observed. For simplicity, the linear conductance was therefore chosen for further investigations.

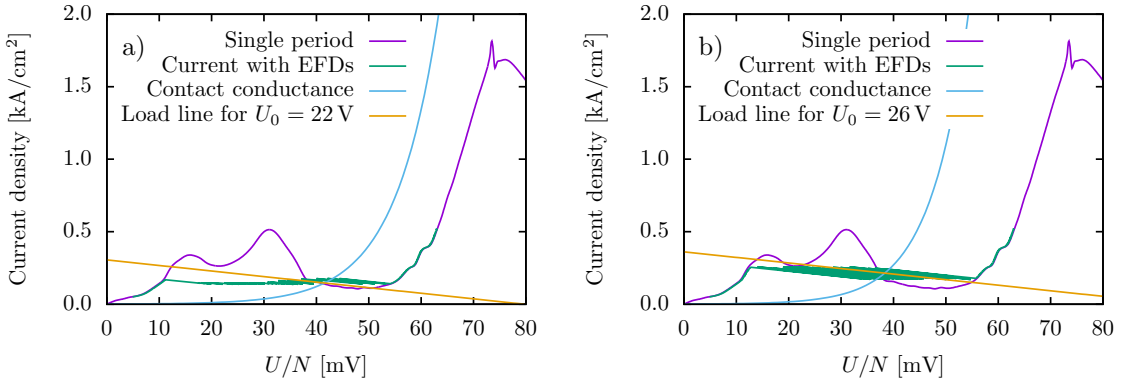

Figure 5.14: The purple line is the current as a function of bias for a single period of the QCL from NEGF simulations. The green line is the current density during a bias sweep up with the EFD program at 50 K. The yellow line is the load line with a resistance of 50 Ω, here shown for a) $U_0 = 22\,\mathrm{V}$, and b) $U_0 = 26\,\mathrm{V}$. The blue line shows the exponential conductance of the injection barrier on the form: $J_{0\to1} = a \cdot e^{b \cdot F_0}$, where a and b where arbitrarily chosen to give the desired shape. For a) $a = 1\mathrm{A/cm}^2$, $b = 0.12/\mathrm{mV}$, and b) $a = 1\mathrm{A/cm}^2$, $b = 0.14/\mathrm{mV}$.

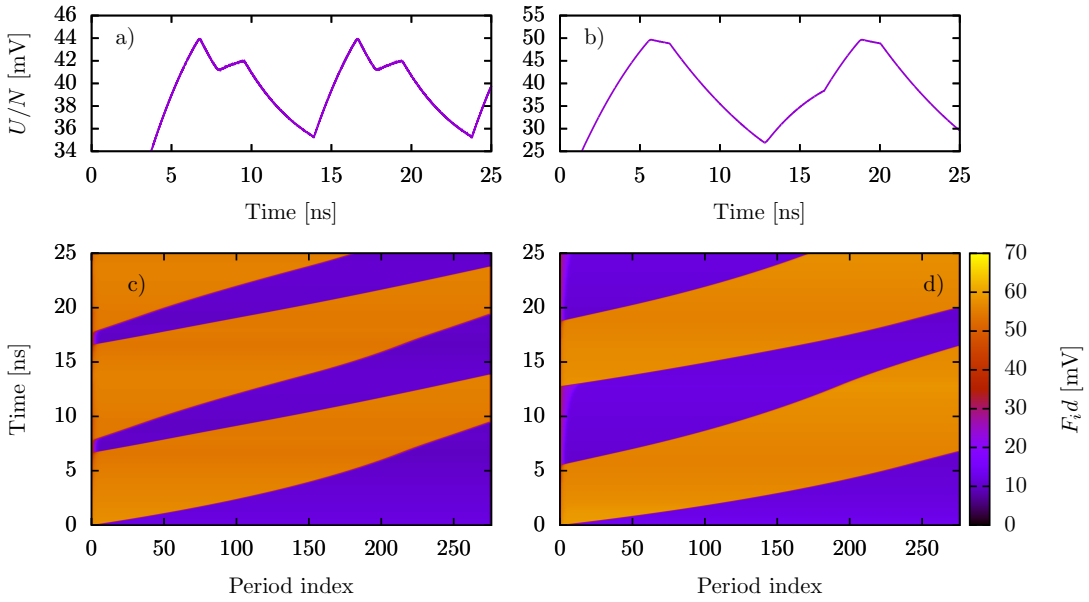

Figure 5.15: The top row shows the average bias per period across the QCL, U/N, as a function of time, for a) $U_0 = 22\,\mathrm{V}$ and the conductance in figure 5.14 a), and b) $U_0 = 26\,\mathrm{V}$ and the conductance in figure 5.14 b). The bottom row shows the local electric field strength as a function of period index and time, for c) $U_0 = 22\,\mathrm{V}$ and the conductance in figure 5.14 a), and d) $U_0 = 26\,\mathrm{V}$ and the conductance in figure 5.14 b). Other parameters are defined as in figure 5.10.

5.4 Compared to Experimental Data

The general shape of figure 5.13 b) roughly resembles the experimental data in figure 5.17 a). Further careful adjustment of the conductance and load line, similar to those in figure 5.12, yielded the bias oscillations in figure 5.16 a). The general shape is in qualitative agreement with experiment. One of the main differences is the small oscillations in both current and bias in the experimental data. However, considering that they occur even after the device is switched off, it might be caused by ripple effects in the power supply or some external capacitance in the circuit.

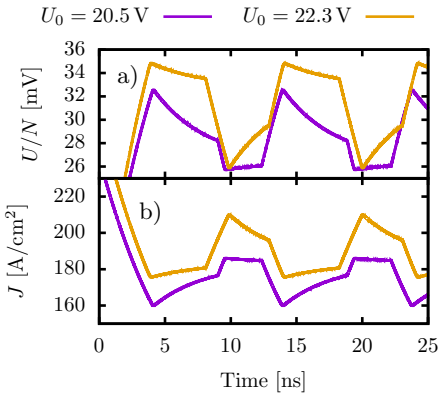

Figure 5.16: a) U/N and b) current density, as a function of time for two different combinations of contact conductance and load line such that they intersect at 35 mV per period.

A quantitative comparison between simulations and experiments reveal some deviations. The period of the bias oscillations in figure 5.17 a) is approximately 60 ns, compared to about 10 ns in the simulations in figure 5.16 a). However, results within an order of magnitude still has to be considered as good results for a couple of reasons. The simulated oscillations occur at significantly lower currents, and as can be seen in figure 5.16, the length of a period seems to increase slightly with the current. Further, the model described in section 2 incorporates approximations for electron densities that deviate from the doping density. For large deviations from the doping densities this approximation might not be sufficient. Such large deviations do indeed occur at the accumulation and depletion fronts, which are crucial for the dynamics of the EFD. Further, equation (2.8) only holds for for $T \gg \pi\hbar^2 n_{i+1}/m^* k_B$. Inserting the doping density and the effective mass for GaAs in the right hand side of the inequality yield a temperature of about 13 K. The approximation should be sufficiently good for 50 K, however it is most likely not good for 10 K.

Another possible source of error is the shape of the current profile within the minimum, corresponding to the main plateau. The NEGF program experienced difficulties in obtaining convergence with respect to the current within this bias region, particularly at low temperatures. Earlier versions of this program has also shown deviations from experimental results within the minimum [17]. If the current within the minimum is underestimated, that could be the sole explanation for not seeing any oscillations in the EFD simulations. Even altering the shape of the minimum could affect the stability and possibly also the behaviour during potential oscillations.

The magnitude of the experimental bias cannot easily be compared to the simulated bias due to the very different current. It should rather be analysed using the current as a function of bias for a single period in e.g. figure 5.12. As the experimental current is about 0.5 kA/cm^2, the low EFD should be at the second current peak, while any high EFD is at a bias corresponding to the same current density at the third peak. The minimum within the experimental bias oscillations is at about 33 mV per period, slightly above the bias of the second current peak. Subtracting a contact bias drop implies that this minimum has a uniform electric field corresponding to the second bias peak. This suggests that, despite very similar bias oscillations, the flat minimum in the experimental bias is caused by the lack of a high EFD, rather than an equal velocity of the accumulation and depletion fronts as is the case of the simulated bias oscillations. Another possibility, which would explain the increasing current within this region, is that a small region near the extraction barrier has a high EFD. If the current is slightly below the second current peak, the boundary between the

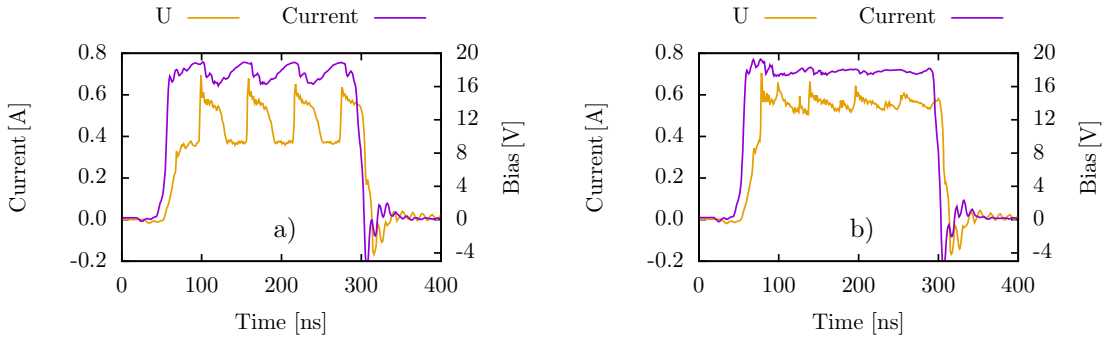

Figure 5.17: Experimental current and bias across the QCL in pulsed mode at 10 K, and with a resistance of 40.7 Ω in series. The data have been extracted from the oscilloscope images in the appendix. These oscilloscope images were provided by Emmanuel Dupont, who also performed the experiments. [14]

domains could travel while the electric field strength within the two domains increases. This would both allow the bias to remain constant and the current to increase.

In some scenarios a uniform field has been observed in simulations to survive for about a nanosecond, before an accumulation or depletion front detaches from the injection barrier. This is significantly shorter than the 30 ns of a uniform electric field that would be required to explain the minimum in figure 5.17 a). The arguments for the different periods of the oscillations given above could also be applied to this case. However, if they are sufficient to explain an order of magnitude difference remains an open question at present. On the other hand, a small high EFD which stabilises after a rapid decrease in bias has only been observed in one scenario, namely in figure 5.8 b). However, the stabilisation of the high EFD is here caused by the disappearance of the low EFD, which is located in between the high and the intermediate EFD. Hence, this behaviour relies on the coexistence of three EFDs, something that can only exist at or below the current of the first current peak.

Figure 5.17 b) shows the experimental bias and current with $U_0 = 43.4$ V. The last three periods of the bias oscillations have clear secondary peaks, and have shapes similar to the simulated bias oscillations in figure 5.13 a). The experimental bias oscillates approximately between 13V and 16V, e.g. the oscillations are of the order 3 V. The simulated oscillations have a magnitude of about 7 mV per period, which yields a total magnitude of about 1.9V. However, it is somewhat unclear how reliable the sharp peaks in the experiments are, as there seems to be a tendency of the experimental bias to overshoot the expected value for rapid changes. The last period in the experimental data is lacking this very sharp peak, and the magnitude of this period is very close to 2 V. The period of the experimental oscillations is also in this scenario about a factor three larger than that of the simulated oscillations. However, the similar shape and magnitude of the oscillations suggests that something similar to figure 5.13 d) might take place inside the QCL.

The experimental current in figure 5.17 a) oscillates between 0.76 A and 0.65 A with an average of about 0.71 A both for the region with the low and the high bias. The low bias region has an average bias estimated to 9.3 V, while the bias of the high bias region is estimated to 14.4 V. Each of them lasts for about 30 ns. The total bias, U_0, is 41.0 V and the resistance that was used is 40.7 Ω. Inserting these values into equation (2.10) yields a bias across the resistor of 26.6 V for the high bias region, and 31.7 V for the low bias region. This corresponds to currents through

the resistor of 0.78 A and 0.65 A, which deviate by 70 mA and 60 mA from the estimated average current, respectively. The current deviation should go into some external capacitance, which is then charged by about 1.9 nAs over the duration of 30 ns. Now, we can estimate the total capacitance of the circuit by $C = q/\Delta U$, where q is the charge. This yields an estimate of 0.37 nF. To put this into perspective, the capacitance of a coaxial cable is typically in the order of 100 pF per meter, and the intrinsic capacitance of the QCL, given by equation (2.14), is 1.8 pF. Clearly, this is a very large capacitance, which has to be located between the resistor and the QCL, as U_0 is constant.

The oscillations in figure 5.17 b) have a significantly smaller magnitude compared to those in figure 5.17 a). However, also these oscillations can be divided into a high and a low bias region, of about 30 ns each. The bias within the high and low bias region was estimated to 14.8 V and 13.6 V respectively, which correspond to currents of 70 mA and 73 mA. The current showed relatively small fluctuations around 71 mA. Using this for estimating the capacitance yield 0.37 nF, in very good agreement with the estimate for figure 5.17 a). Although the calculated capacitance from the two plots in figure 5.17 were in good agreement, it should only be viewed as a very rough estimate. This estimated capacitance was to be used for simulations with an external capacitance in the following section.

6 Impact of Capacitance on Pulsed Mode Operation

Introducing an external capacitance causes some ambiguity in what the measured current is. The two extreme possibilities are the current through the resistor, J, and the current going into the QCL, $J - \frac{C_{\text{ext}}}{A}\frac{dU}{dt}$. However, since the considered capacitance represents some parasitic capacitance in the circuit, some intermediate value could also be measured depending on where the external capacitance is located in relation to where the current is measured. For simplicity, only the extremes are presented in this section. J shall be referred to as the *resistor current*, while $J - \frac{C_{\text{ext}}}{A}\frac{dU}{dt}$ shall be referred to as the *QCL current*.

6.1 Pulsed Mode with a High Conductance

In this section, the stable domains within the main plateau are simulated with a good injection barrier conductance. Pulsed mode is imitated by only evaluating a single bias at a time, and by starting with $U(t{=}0) = 0$. Figure 6.1 shows the U/N, resistor current, and QCL current with an external capacitance of 0 pF, 50 pF, 370 pF, and 2 nF respectively. Introducing an external capacitance causes fluctuations of the QCL current during an extended period of time. In all

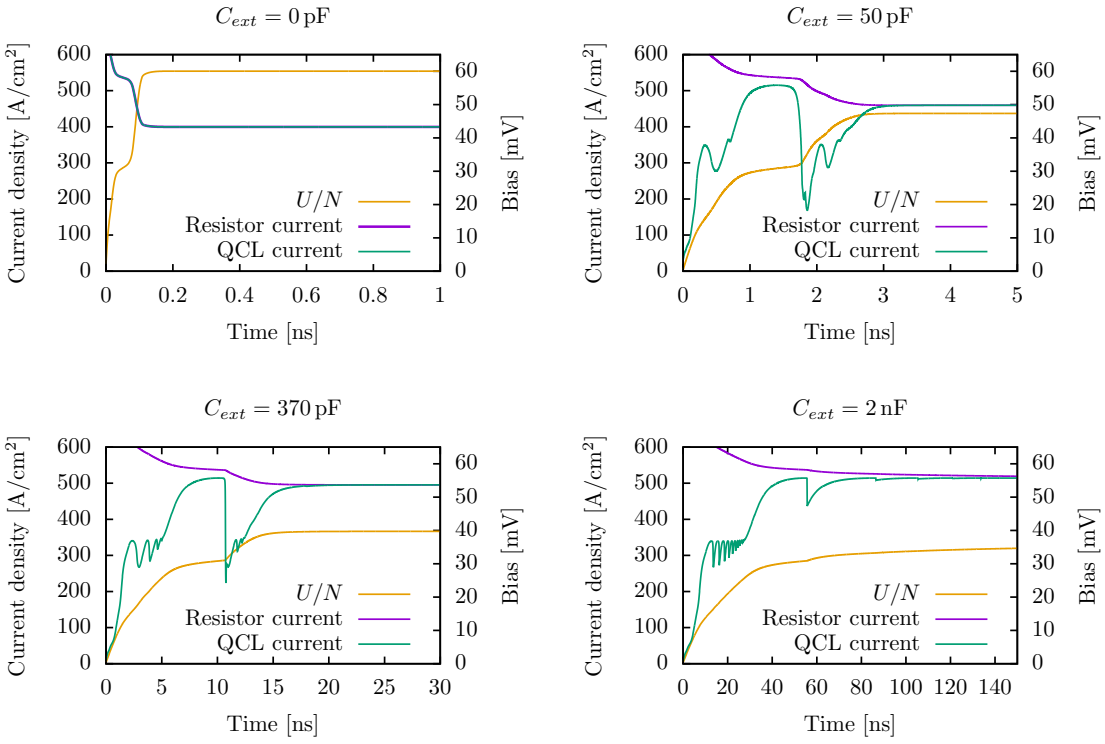

Figure 6.1: Pulsed mode is simulated by starting with U=0. A good contact conductance of $\sigma/A = 50\,\text{A}\,\text{mV}^{-1}\text{cm}^{-2}$ is used, a resistance of 40.7 Ω, a total bias $U_0 = 40$ V, and an external capacitance of a) 0 pF, b) 50 pF, c) 370 pF, and d) 2 nF.

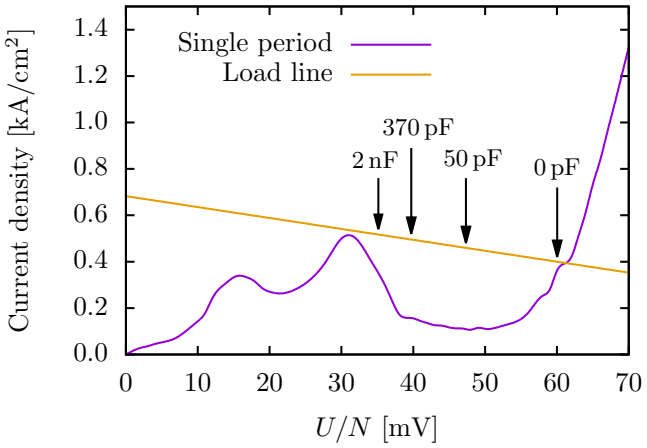

Figure 6.2: The purple line is the current as a function of bias for a single period of the QCL. The yellow line is the load line with $U_0 = 40\,\mathrm{V}$, and a resistance of $40.7\,\Omega$. The arrows show the bias at which the QCL stabilises in pulsed mode with different external capacitances.

scenarios it does stabilise after a certain time, which depends heavily on the external capacitance. With an external capacitance of 2 nF, the shape of the QCL current looks like that of a bias sweep up, with the oscillations at the first plateau resolved in time. Although less prominent, the same features can be seen with 50 pF, and 370 pF. With 2 nF, bias drops at what would correspond to the main plateau resembles those with the bias controlled conditions, shown in figure 5.1 a). This is perhaps not too surprising, considering the large capacitance which suppresses bias fluctuations. It seems that, similarly to that introducing a load line creates conditions in between a controlled bias and a controlled current, introducing an external capacitance creates conditions in between a load line and a controlled bias.

It is noteworthy how different the final bias is, for the different capacitances in figure 6.1. Therefore, the final bias is pointed out with the arrows in figure 6.2. Without an external capacitance, the current is reduced so rapidly that only a very small low EFD can form. This indicates that the ability to resolve the plateau in pulsed mode is a feature of the external capacitance. Without the external capacitance, this bias region would only appear as a discontinuity. Intentionally connecting an external capacitance might improve the ability to resolve the domain states in experiments with pulsed mode operation.

6.2 Oscillations with a Low Conductance

Figure 6.3 shows the bias and current fluctuations with a reduced contact conductance and an external capacitance. The left column shows the fluctuations with the same conditions as figure 5.13 a) but with an external capacitance of 50 pF and 370 pF, respectively, while the right column shows the fluctuations with the parameters as in figure 5.13 b), with an external capacitance of 50 pF and 370 pF. In every case in figure 6.3, both the bias and the resistor current are much more stable compared to those in section 5.3, while the QCL current shows rapid fluctuations similar to the bias in figure 5.17. In fact, that a large total capacitance reduces bias fluctuations can be directly seen from equation (2.16). This is in direct contradiction to the experimental data in figure 5.17. Hence, the parasitic capacitance cannot alone explain why the measured current and bias do not fulfil equation (2.10).

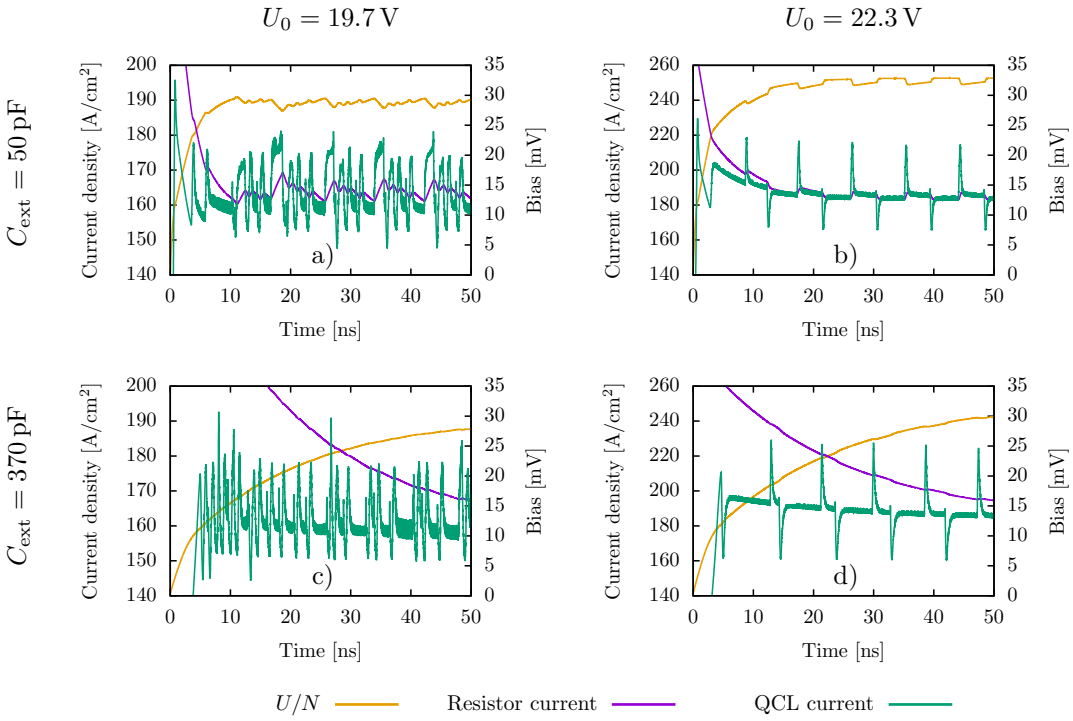

Figure 6.3: U/N, resistor current, and QCL current as a function of time. a) and c): parameters as in 5.13 a) with an external capacitance of a) 50 pF and c) 370 pF. b) and d): parameters as in 5.13 b) with an external capacitance of b) 50 pF and d) 370 pF.

7 Summary and Outlook

A theoretical model for describing electron transport in a superlattice has been studied, adapted for QCLs, and also extended to accurately simulate the QCL under conditions as used in experiments. The model has been implemented in a `C++` program, designed for simulating EFD dynamics in QCLs. The program is a starting point for investigating EFD dynamics, and could be extended to include other parameters and simulate the impact of these parameters on the properties of the QCL.

Simulations have been performed using the EFD program to investigate the fundamental behaviour of EFDs using different models for the experimental circuit. The results have been compared to experimental data and analysed thoroughly, both qualitatively and quantitatively. The impact on the EFDs by various parameters, such as the load line resistance, contact conductance and an external capacitance, has been investigated and analysed.

By using the numerical model studied here, many experimental observations could be reproduced. The stable domains that are observed in experiments at higher temperatures were successfully reproduced in simulations. The oscillations at low temperatures could not be observed directly at the main plateau. However, reducing the contact conductance induced oscillations with similar behaviour. Many different characteristic bias and current oscillations have been observed, and also explained from the shape of the EFDs. These oscillations could be used as references for explaining similar oscillations in experiments.

The velocities of accumulation and depletion fronts within the QCL have also been studied. The velocities have been shown to depend strongly on a combination of contact conductance and bias, while a very week dependence was observed on an altered bias alone. The change in velocities could possibly be attributed to the change in current, as the conductance and bias was altered such that the current should change while attempting to maintain the bias.

A significant impact of an external capacitance on pulsed mode operation has been observed. Simulated results suggests that a greater external capacitance could improve the ability to resolve plateaus caused by formation of EFDs. Further, a large external capacitance suppresses bias fluctuations during oscillations, while inducing rapid fluctuations in current.

Further improvements to the model are possible, in order to obtain more accurate simulations. The estimated current within the accumulation and depletion regions could be improved. A somewhat better approximation would be to use the full expression in equation (2.7), which would not be particularly heavy. Another possibility would be to simulate the QCL with increased or reduced number of carriers in the NEGF program. This would most likely yield a much better approximation for the current within the accumulation and depletion fronts. Further, accounting for the position of the charge accumulation at different field strengths would yield a more realistic behaviour of the boundary.

As these simulations are currently not particularly computational heavy, not too much effort has been put into optimisation. However, as noted for figure 4.3, there is a very different time scale of the travelling boundary and when the boundary is replaced by a new one. This is similar to a stiff numerical problem, where a very fine step size is require within a certain region, while for a the majority of the simulation a much greater step size is sufficient. Therefore, a dynamic step size could most likely reduce the computational time significantly, for oscillating domains with maintained accuracy.

If a single period of a QCL was grown, the current for a single period of the QCL could be measured directly in experiments. Using such an experimental current in the EFD program would provide a direct way of comparing the dynamics of EFDs in experiments and simulations. This would be a helpful tool for increasing the accuracy of the model, and evaluating the accuracy of the approximations that were made.

The minimum of the current as a function of bias cannot be resolved in experimental measurements due to domain formation. Therefore, it is difficult to evaluate the accuracy of the NEGF program within these regions. However, due to the dynamics of EFDs being sensitive to the width and depth of the minimum, the EFD program could serve as a tool for evaluating the accuracy of the NEGF program within these regions. This assumes that the model in the EFD program is sufficiently accurate. Most likely the EFD program would have to be improved in conjunction with the NEGF program to replicate the behaviour of the EFDs that is observed in experiments.

One of the main motivations for investigating the dynamics of EFDs is to be able to draw conclusions of how they will impact the performance of the QCL. There has been evidence suggesting that THz QCLs, similar to that which has the highest operating temperature, ignites in a EFD state [18]. E.g. EFDs are present when the laser gain in the medium starts to outweigh the losses in the cavity. By performing NEGF simulations at both different biases and wave guide intensities, and use the current and gain as input to the EFD program, the intensity inside the wave guide could be included in the simulations. This could allow for actively designing a QCL structure for igniting in a state of EFD, which is an intriguing possibility that may have the potential to further increase the maximum operational temperature of THz QCLs.

References

[1] L. Esaki and R. Tsu. Superlattice and negative differential conductivity in semiconductors. *IBM J. Res. Dev.*, 14:61, 1970.

[2] J. Faist, F. Capasso, D. L. Sivco, C. Sirtori, A. L. Hutchinson, and A. Y. Cho. Quantum cascade laser. *Science*, 264:553–556, 1994.

[3] S. Fathololoumi, E. Dupont, C.W.I. Chan, Z.R. Wasilewski, S.R. Laframboise, D. Ban, A. Mátyás, C. Jirauschek, Q. Hu, and H. C. Liu. Terahertz quantum cascade lasers operating up to $\sim$ 200 K with optimized oscillator strength and improved injection tunneling. *Opt. Express*, 20(4):3866–3876, Feb 2012.

[4] Andreas Wacker. Semiconductor superlattices: a model system for nonlinear transport. *Phys. Rep.*, 357(1):1 – 111, 2002.

[5] Luis L Bonilla and Holger T Grahn. Non-linear dynamics of semiconductor superlattices. *Rep. Prog. Phys.*, 68(3):577, 2005.

[6] A. Wacker, M. Lindskog, and D. Winge. Nonequilibrium greens function model for simulation of quantum cascade laser devices under operating conditions. *IEEE J. Sel. Top. Quantum Electronics*, 19(05), 2013.

[7] A. Wacker and E. Schöll. Criteria for stability in bistable electrical devices with S- or Z-shaped current voltage characteristic. *J. Appl. Phys.*, 78:7352, 1995.

[8] E. Dupont, S. Fathololoumi, Z. R. Wasilewski, G. Aers, S. R. Laframboise, M. Lindskog, S. G. Razavipour, A. Wacker, D. Ban, and H. C. Liu. A phonon scattering assisted injection and extraction based terahertz quantum cascade laser. *J. Appl. Phys.*, 111(7):73111, 2012.

[9] S. L. Lu, L. Schrottke, S. W. Teitsworth, R. Hey, and H. T. Grahn. Formation of electric-field domains in GaAs - $Al_xGa_{1-x}As$ quantum cascade laser structures. *Phys. Rev. B*, 73(3):033311, Jan 2006.

[10] M. Wienold, L. Schrottke, M. Giehler, R. Hey, and H. T. Grahn. Nonlinear transport in quantum-cascade lasers: The role of electric-field domain formation for the laser characteristics. *J. Appl. Phys.*, 109(7), 2011.

[11] Rudra Sankar Dhar, Seyed Ghasem Razavipour, Emmanuel Dupont, Chao Xu, Sylvain Laframboise, Zbig Wasilewski, Qing Hu, and Dayan Ban. Direct nanoscale imaging of evolving electric field domains in quantum structures. *Scientific Reports*, 4, 2014.

[12] Andreas Wacker. Private communication, 2016.

[13] Luis L. Bonilla. Periodic generation and propagation of traveling fronts in dc voltage biased semiconductor superlattices. *SIAM Journal on Applied Mathematics*, 57(6):1588–1614, 1997.

[14] Emmanuel Dupont. Private communication, 2016.

[15] J. Richard Christman. *Fundamentals of Solid State Physics*. Wiley, 1988.

[16] Leonard J. Brillson. *Contacts to Semiconductors: Fundamentals and Technology.* William Andrew, 1994.

[17] M. Lindskog, D. O. Winge, and A. Wacker. Injection schemes in THz quantum cascade lasers under operation. *Proc. SPIE*, 8846:884603, 2013.

[18] S. Fathololoumi, E. Dupont, Z. R. Wasilewski, C. W. I. Chan, S. G. Razavipour, S. R. Laframboise, Shengxi Huang, Q. Hu, D. Ban, and H. C. Liu. Effect of oscillator strength and intermediate resonance on the performance of resonant phonon-based terahertz quantum cascade lasers. *J. Appl. Phys.*, 113(11):–, 2013.

Appendix A: Interpolation Algorithms

The current profile used for the performance analysis in this section is taken from NEGF simulations of a QCL, with phonon assisted injection and extraction [8], at 50K. A linear interpolation simply draws a straight line between two adjacent points. The cubic interpolation uses the nearest four data points and construct a third degree polynomial that goes through each point. This yields a significant improvement to linear interpolation, however it still has significant discontinuities in its derivative as can be seen in figure 7.1. Cubic splines is a somewhat more sophisticated algorithm, that constructs a third degree polynomial for interval such that the second derivative is continuous at the boundary. This yields a perfectly smooth first derivative, as can be seen.

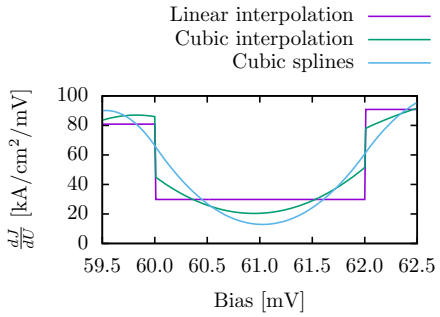

Figure 7.1: Derivative of the current density with respect to bias.

The smoothness of the current profile does play a vital role in simulations of electric field domains, primarily for reaching a stable configuration of EFDs with as few computations as possible. Cubic interpolation and cubic splines has been compared for simulations of EFDs in the bias range from 27 mV to 35 mV. Cubic splines showed a 20% reduction in the average number of iterations required to reach stable EFDs as compared to cubic interpolation. Further, simulations within the same interval was done in half the time compared to cubic interpolation, showing that it not only requires fewer iterations but also fewer computations per iteration.

Appendix B: Experimental Data

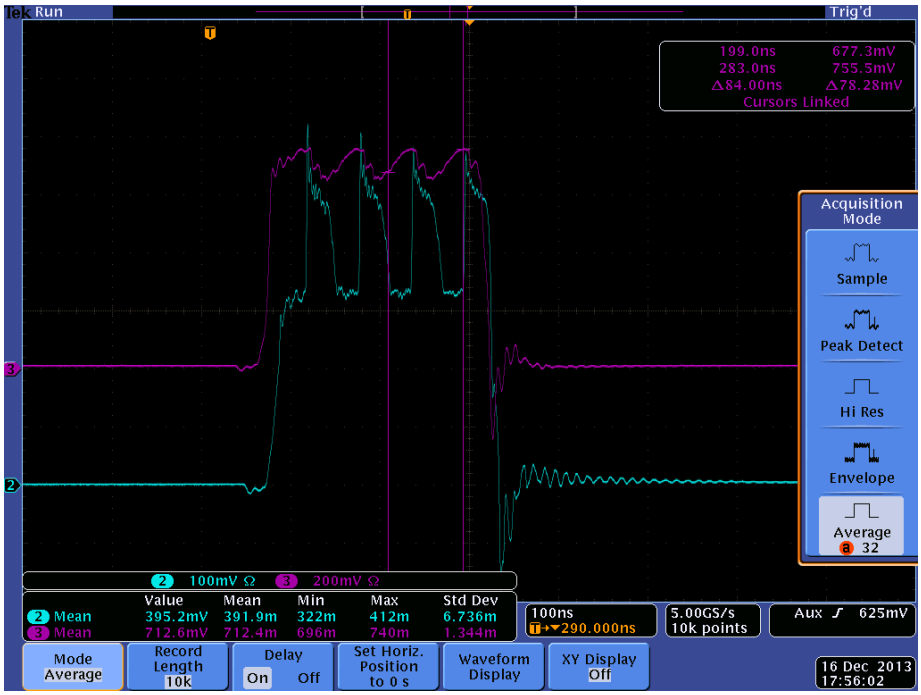

Figure 7.2: Oscilloscope image of the current (magenta) and bias (cyan) of the V843 sample in pulsed mode at 10 K and $U_0 = 41.0$ V. Provided by Emmanuel Dupont [14].

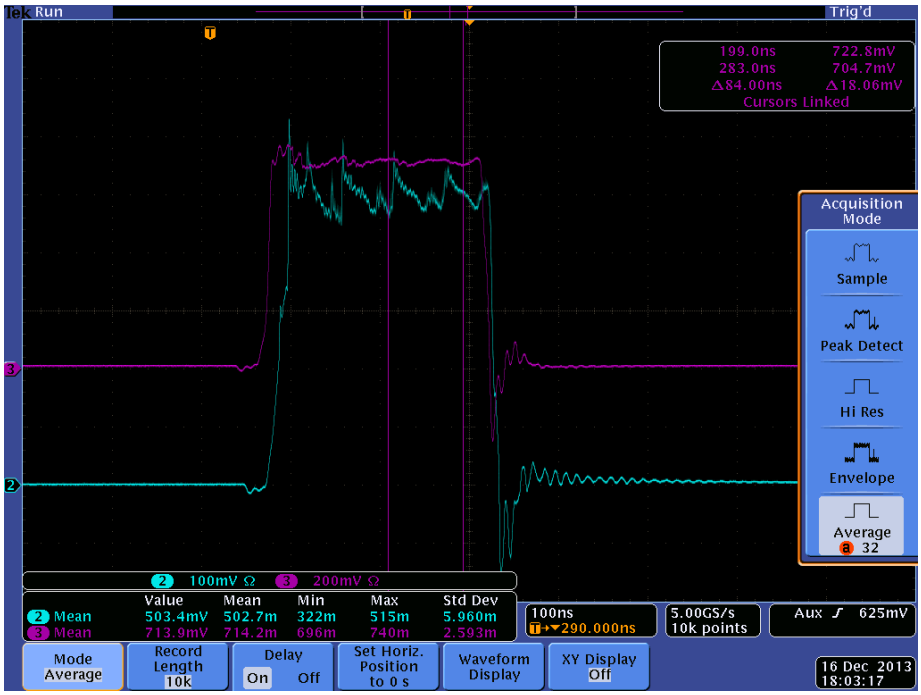

Figure 7.3: Oscilloscope image of the current (magenta) and bias (cyan) of the V843 sample in pulsed mode at 10 K and $U_0 = 43.4$ V. Provided by Emmanuel Dupont [14].